

Gas outflows in two recently quenched galaxies at $z = 4$ and 7

F. Valentino^{1,2,3}, K. E. Heintz^{1,4,5}, G. Brammer^{1,4}, K. Ito^{1,2,6}, V. Kokorev⁷, K. E. Whitaker^{8,1}, A. Gallazzi⁹, A. de Graaff¹⁰, A. Weibel⁵, B. L. Frye¹¹, P. S. Kamienieski¹², S. Jin^{1,2}, D. Ceverino^{13,14}, A. Faisst¹⁵, M. Farcy¹⁶, S. Fujimoto⁷, S. Gillman^{1,2}, R. Gottumukkala^{1,4}, M. Hamadouche⁸, K. C. Harrington^{17,18,19,20}, M. Hirschmann^{16,21}, C. K. Jespersen²², T. Kakimoto^{23,24}, M. Kubo²⁵, C. d. P. Lagos^{26,27,1}, M. Lee^{1,2}, G. E. Magdis^{1,2}, A. W. S. Man²⁸, M. Onodera^{24,29}, F. Rizzo³⁰, R. Shimakawa³¹, D. J. Setton³², M. Tanaka^{23,24}, S. Toft^{1,4}, P.-F. Wu³³, and P. Zhu^{1,2}

(Affiliations can be found after the references)

Received –; accepted –

ABSTRACT

Outflows are a key element in the baryon cycle of galaxies, impacting their evolution by extracting gas, momentum, energy, and then injecting them into the surrounding medium. The properties of gas outflows provide a fundamental test for our models of how galaxies transition from a phase of active star formation to quiescence. Here we report the detection of outflowing gas signatures in two recently quenched, massive ($M_{\star} \sim 10^{10.2} M_{\odot}$) galaxies at $z = 4.106$ (NS_274) and $z = 7.276$ (RUBIES-UDS-QG-z7) observed at rest-frame ultra-violet (UV) to near-infrared wavelengths with JWST/NIRSpec. The outflows are traced by blue-shifted magnesium (MgII) absorption lines, and in the case of the $z = 4.1$ system, also by iron (FeII) and sodium (NaI) features. Together, these transitions broadly trace the chemically enriched neutral phase of the gaseous medium. The rest-frame optical spectra of the two sources are similar to those of local post-starburst galaxies, showing deep Balmer stellar features, relatively low D_n4000 index, and minimal ongoing star formation on 10 Myr timescales as traced by the lack of bright nebular and recombination emission lines, also suggesting the absence of a strong and radiatively efficient AGN activity. The galaxies' star formation histories are consistent with a recent and abrupt quenching of star formation, which continued at rates of $\sim 15 M_{\odot} \text{ yr}^{-1}$ averaged over the last 100 Myr of their life. In the case of NS_274, dedicated millimeter observations allow us to strongly constrain also the dust obscured SFR to $< 12 M_{\odot} \text{ yr}^{-1}$, unambiguously confirming its quiescence. Under simple geometrical assumptions, we derive mass loading factors $\eta = \dot{M}_{\text{out}}/\text{SFR}_{100\text{Myr}} \lesssim 1$ and ~ 50 for the $z = 4.1$ and $z = 7.3$ systems, respectively, and similarly different energy carried by the outflows ($\dot{E}_{\text{out}} \lesssim 5 \times 10^{40}$ and $\sim 2 \times 10^{42} \text{ erg s}^{-1}$). Supernovae feedback can account for the mass and energy of the outflow in NS_274. However, the low mass loading factor and average gas velocity ($\sim 180 \text{ km s}^{-1}$, lower than the stellar velocity dispersion) suggest that the observed outflow is unlikely to be the primary reason behind the quenching of NS_274, but it might represent a relic of the star formation process winding down. Star formation-related processes seem to be also insufficient to explain the extreme mass outflow rate of RUBIES-UDS-QG-z7, which would require an additional ejective mechanism such as an undetected AGN. Finally, the average outflow velocities per unit stellar mass, SFR, or its surface area are consistent with those of lower-redshift post-starburst galaxies, suggesting that outflows in rapidly quenched galaxies might in substance occur similarly across cosmic time. Our findings hint at the existence of a rich tapestry of galaxy quenching pathways at high redshift, and they remark the importance of large spectroscopic samples mapping different spectral features to account for the different timescales on which different mechanisms contribute to this process.

Key words. Galaxies: evolution, high-redshift, stellar content; ISM: jets and outflows.

1. Introduction

The physical mechanisms responsible for the suppression of star formation in galaxies remain a major topic of debate in modern astrophysics, especially after the spectroscopic confirmation of massive (stellar masses of $M_{\star} \sim 10^{10-11} M_{\odot}$) “quenched” systems in the first few hundred million years ($z \sim 3 - 7$) of our Universe’s history (Glazebrook et al. 2017; Schreiber et al. 2018a; Tanaka et al. 2019; Valentino et al. 2020; Forrest et al. 2020a,b, 2022; Antwi-Danso et al. 2023, 2025; Carnall et al. 2023, 2024; Nanayakkara et al. 2024; Glazebrook et al. 2024; de Graaff et al. 2024b; Urbano Stawinski et al. 2024; Tanaka et al. 2024; Kakimoto et al. 2024; Weibel et al. 2024a; Baker et al. 2024; Onoue et al. 2024; Kokorev et al. 2024 among others). Models and simulations have to invoke powerful winds and gas ejection powered by active galactic nuclei (AGN) in order to reproduce stellar masses and stellar mass functions at $z = 0$, with a lesser role played by star formation feedback especially at the highest masses (see the reviews by Somerville & Davé 2015; Naab & Ostriker 2017). However, despite the huge effort to refine the feedback recipes implemented in models, the number density and stellar masses of quenched galaxies at $z > 3$ re-

present a challenge in most, if not all state-of-the-art cosmological simulations (e.g., Schreiber et al. 2018a; Merlin et al. 2019; Valentino et al. 2020, 2023; De Lucia et al. 2024; Lagos et al. 2024).

The exact details of the physical models of AGN and stellar feedback differ from simulation to simulation, but outflows remain a staple mechanism to quench galaxies in most, if not all available models (Kurinchi-Vendhan et al. 2024; Lagos et al. 2024). Different recipes and implementations might result in equally robust stellar mass functions in the local Universe, but they predict different outflow properties – which thus become a powerful tool to gain insight into the physics governing galaxies. Observationally, multiphase gas flowing outwards from star-forming galaxies or systems harboring actively growing supermassive black holes is well documented especially up to cosmic noon, based on the detection of both emission and absorption lines across the whole electromagnetic spectrum (e.g., Förster Schreiber & Wuyts 2020; Veilleux et al. 2020). Focusing on the colder and denser outflow phases, the detection of low ionization absorption features in the rest-frame ultra-violet (UV) spectrum of galaxies has been a chief probe of their properties (e.g., Frye

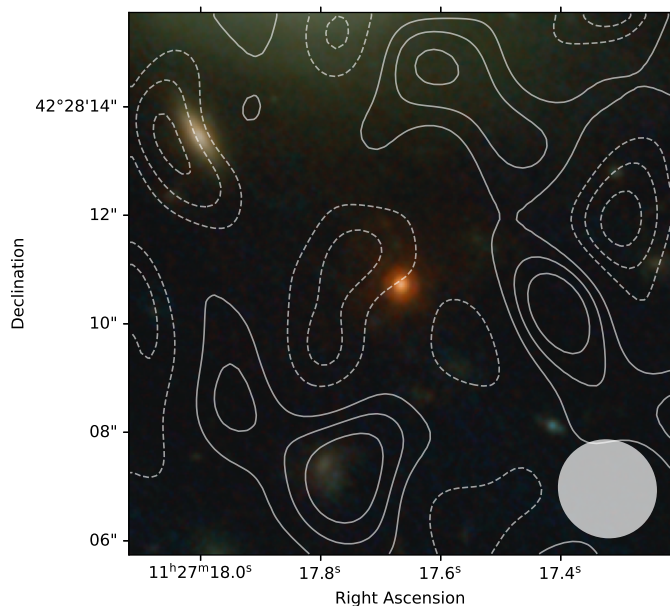


Fig. 1. RGB color image of NS_274 at $z = 4.1061$ overlaid with NOEMA 1.3 mm contours. The $10'' \times 10''$ background image is a color-composite of 6 available wide-band NIRCcam filters. The dashed and solid white contours indicate the $[-3\sigma, -2\sigma, -1\sigma, 1\sigma, 2\sigma, 3\sigma]$ dust continuum emission at $260 \mu\text{m}$ rest-frame from NOEMA observations. The elliptical patch indicated the NOEMA beam.

et al. 2002; Shapley et al. 2003; Rupke et al. 2005; Veilleux et al. 2005; Weiner et al. 2009; Rubin et al. 2014; Veilleux et al. 2020; Xu et al. 2022; Mingozzi et al. 2022). This allowed for mapping the outflow properties across a large dynamic range of host galaxy properties and establishing various scaling relations (e.g., average and maximum outflow velocity vs stellar mass, star formation rate SFR, or their surface densities; see Davis et al. 2023, and references therein).

In massive systems, the mixture of intense star formation and simultaneous growth of central black holes makes the outflows phenomenon more complicated to decipher. Moreover, studying the population of recently quenched systems that likely experienced the effects of both supernovae (SNe) and AGN-powered feedback in their recent past, and are on their way to quiescence, has been a particularly difficult task to undertake, given their relative rarity after cosmic noon and faintness at UV wavelengths. In general, most observational studies ascertained the presence of outflowing gas in recently quenched systems, both in presence or absence of ongoing AGN activity (e.g., Tremonti et al. 2007; Coil et al. 2011; Maltby et al. 2019; Baron et al. 2020, 2022; Man et al. 2021; Davis et al. 2023; Taylor et al. 2024).

At higher redshifts, when approaching the main epoch of quenching of the most massive systems, galaxies showing typical “post-starburst” signatures such as deep Balmer absorption lines, shallow D_n4000 breaks, and weak emission lines, naturally become more common (D’Eugenio et al. 2020; Forrest et al. 2020b). This makes the study of this population more appealing and urgent – and, thanks to JWST, also feasible. Interestingly, AGN seem to be common in recently quenched galaxies at $z = 2 - 3$ and above. Extreme optical line ratios, broad emission features and mid-infrared detections are routinely reported (e.g., Carnall et al. 2023; Onoue et al. 2024; Ji et al. 2024). Ionized outflows only (e.g., Kubo et al. 2022) are unlikely to be sufficient to quench the star formation, but, recently, signatures of massive amounts of neutral gas leaving

quenched galaxies at $z = 2 - 3$ have been reported in the literature (D’Eugenio et al. 2023; Belli et al. 2024; Davies et al. 2024). The simultaneous presence of high-velocity ($\sim 1000 \text{ km s}^{-1}$) neutral outflows and AGN signatures has been interpreted as the smoking gun of a causal connection between the activity of supermassive black holes and quenching. However, the contribution to the mass and energy budget of cold outflows due to the last episode of star formation or its residuals is yet to be fully understood. This is especially true in the presence of outflows less extreme in terms of velocity and mass.

In this work, we study two distant and recently quenched galaxies showing signatures of outflowing gas: NS_274 at $z = 4.106$ and RUBIES-UDS-QG-z7 at $z = 7.276$. Their redshifts have been first confirmed with JWST/NIRSpec observations in Frye et al. (2024) and Weibel et al. (2024a), respectively. These two sources stand out as the most distant quenched galaxies with high S/N coverage of the rest-frame UV and optical spectra at medium and high spectral resolution in our archival search and dedicated survey with JWST/NIRSpec (“DeepDive” project, Ito et al. in prep.). They thus allow us to explore a new redshift regime, while future work on population studies at lower redshifts ($z \sim 2 - 3$) will follow. In particular, in this work we confirm and refine the redshift of RUBIES-UDS-QG-z7 thanks to newly acquired data with a G235M/F170LP grating/filter combination and a custom reduction pipeline that is able to recover the whole wavelength coverage allowed by the long-pass filter and position on the detector (Brammer et al. in prep.). Here we mainly focus on the iron (Fe) and magnesium (Mg) absorption features in the rest-frame UV and their blue-shifts, signposting the presence of cold outflowing gas. In addition, we independently re-analyze the properties of NS_274, which has been presented in Wu (2024), and incorporate information from the sodium doublet Na I D at rest-frame optical wavelengths.

Throughout this work, we make use of the AB system to report magnitudes. We adopt a Λ CDM cosmology with $\Omega_m = 0.3$, $\Omega_\Lambda = 0.7$, and $H_0 = 70 \text{ km s}^{-1} \text{ Mpc}^{-1}$.

2. Data

2.1. Imaging

NS_274¹ lies behind the galaxy cluster PLCK G165.7+67.0 at $z = 0.35$ (G165 in brief). This field was imaged as part of the JWST Prime Extragalactic Areas for Reionization and Lensing Science (PEARLS) Guaranteed Time Observations (GTO; PID 1176, PI: R. Windhorst). Follow-up Near Infrared Camera (NIR-Cam, Rieke et al. 2023) imaging and Near Infrared Spectrograph (NIRSpec, Jakobsen et al. 2022) spectroscopy was acquired in a JWST Disruptive Director’s Time (DDT) program (PID 4446; PI: B. Frye; see Frye et al. 2024 for the analysis of all JWST observations in this field). This field also benefits from ample ancillary data, such as Hubble Space Telescope (HST) in WFC3-IR imaging (GO-14223; PI: B. Frye, Frye et al. 2019), Very Large Array (VLA) observations (Pascale et al. 2022), XMM-Newton observations (AO22, #92030; PI: B. Frye), and large ground-based telescope observations (see Frye et al. 2024; Kamienski et al. 2024 for a full description; Cañameras et al. 2018 for previous work on this field). For the purpose of this work, we utilized

¹ The spectroscopic follow-up was primarily designed to characterize the multiply lensed supernova “SN H0pe” presented in Frye et al. (2024). For our target, we adopt the name it has in this work.

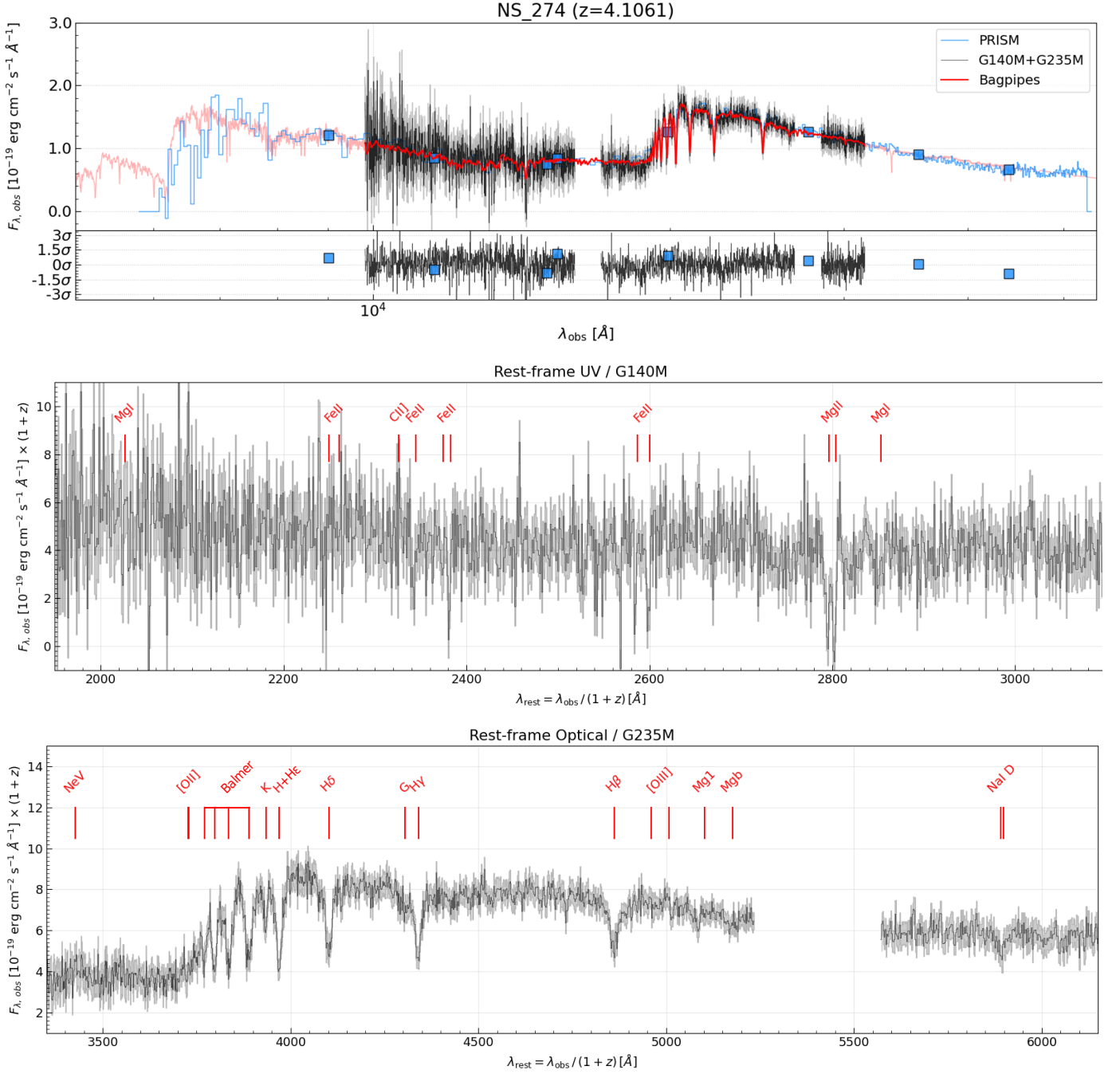


Fig. 2. Spectra, photometry, and SED modeling of NS_274 at $z = 4.1061 \pm 0.0003$. *Top:* Here we indicate the photometry (blue squares), JWST/NIRSpec medium resolution spectra (G140M+G235M, black line), and their uncertainties (gray line) that we jointly modeled with Baggpipes (red line) in the observed frame. The normalized residuals of the modeling are shown in the lower inset. For reference, we also show the PRISM spectrum (blue). *Center:* rest-frame UV spectrum covered by the G140M grating. *Bottom:* rest-frame optical spectrum covered by the G235M grating. We mark in red the expected location of emission and absorption lines at the derived systemic redshift $z_{\text{spec}} = 4.1061$, as labeled. The flux densities in the bottom panels have been rescaled by $(1+z)$ to conserve the energy.

the available JWST and HST imaging in 8 bands covering the 0.9–4.4 μm range. The images were retrieved from the DAWN JWST Archive (DJA)² and homogeneously reduced with GRIZLI (Brammer 2023) as described in Valentino et al. (2023). The photometry was extracted on a combined image (mosaic version v7.0) of the available NIRCcam/Long Wavelength (LW) filters in circular apertures (0.5" diameter) with the pythonic ver-

sion of SourceExtractor (Bertin & Arnouts 1996; Barbary 2016) and corrected to total within an elliptical Kron aperture (Kron 1980). The aperture correction is computed on the LW combined image and applied to all bands (Valentino et al. 2023). Moreover, we corrected for the minimal extinction of the Milky Way ($E(B - V) = 0.0165$) based on the maps in Schlafly & Finkbeiner (2011). For reference, the observed magnitude in the F200W filter ($m_{\text{F200W,AB}} = 23.34 \pm 0.05$) is consistent with previously reported estimates (Frye et al. 2024; Wu 2024). Finally,

² <https://dawn-cph.github.io/dja/index.html>

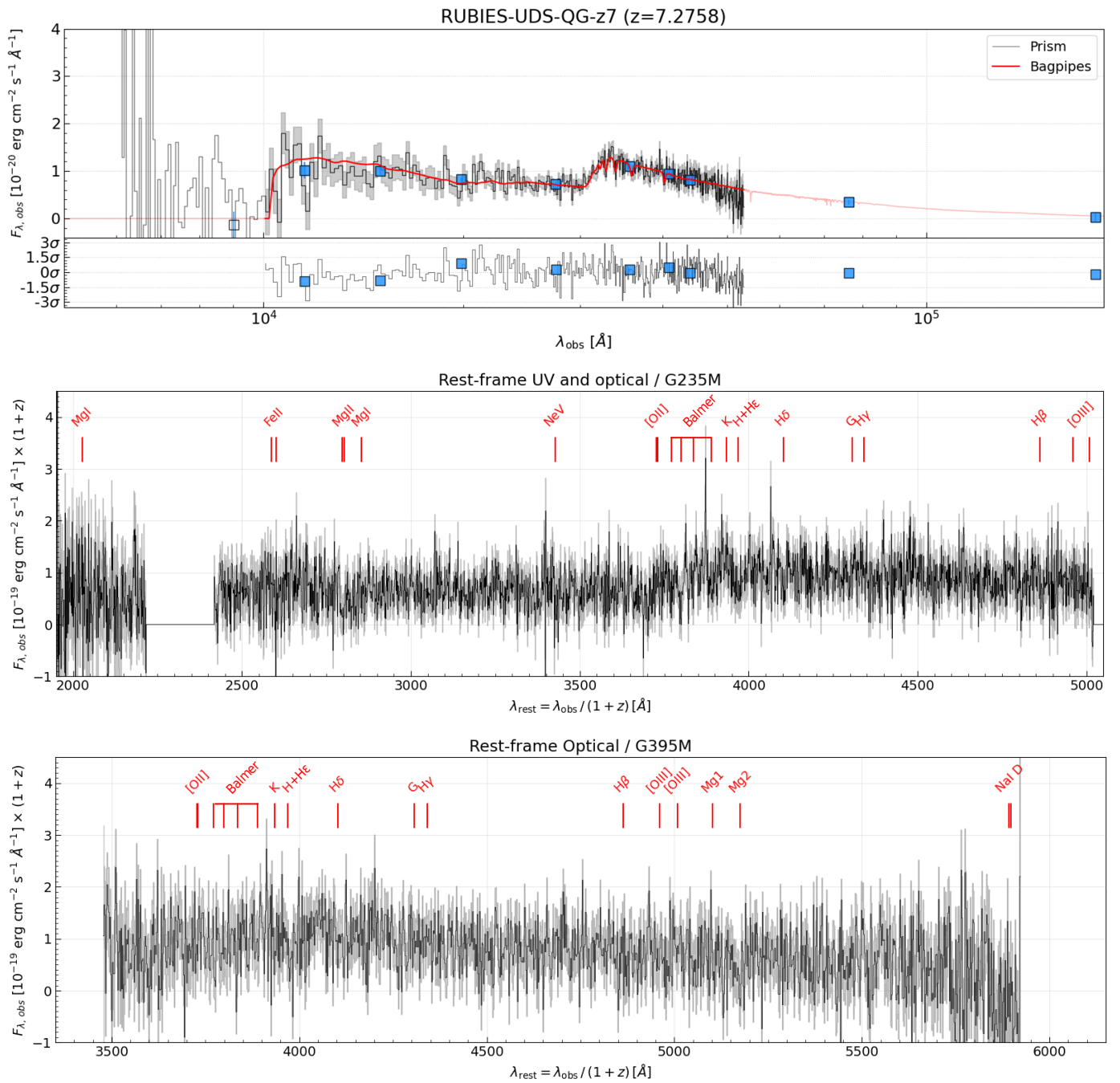


Fig. 3. Spectra, photometry, and SED modeling of RUBIES-UDS-QG-z7 at $z = 7.2758 \pm 0.0011$. *Top:* Here we indicate the photometry (blue squares), the JWST/NIRSpec PRISM spectrum (black line), and its uncertainty (gray line) that we jointly modeled with Bagpipes (red line) in the observed frame. The normalized residuals of the modeling are shown in the lower inset. *Center:* rest-frame UV spectrum covered by the extended G235M grating. *Bottom:* rest-frame optical spectrum covered by the G395M grating. We mark in red the expected location of emission and absorption lines at the derived systemic redshift $z_{\text{spec}} = 7.2758$, as labeled. The flux densities in the bottom panels have been rescaled by $(1+z)$ to conserve the energy.

we checked for the gravitational lensing effect of the cluster at the location of NS_274, finding a mild magnification correction of $\mu = 2.0 \pm 0.2$ in the recent maps by [Kamieneski et al. \(2024\)](#) – without strongly distorting the shape.³

In addition to optical and near-infrared imaging, we obtained coverage of NS_274 at 1.3 mm (260 μm rest-frame) with the Northern Extended Millimetre Array (NOEMA, ID:

³ We note that this target is outside the field of view of the lensed image constraints used in the models ([Frye et al. 2024](#)).

W23CU001, PIs: Gómez-Guijarro & Valentino). The target was observed for 11.6 hours from May to September 2024 in D configuration. The frequency tunings are 212.5–220.0 GHz in the lower sideband (LSB) and 228–235.5 GHz in the upper sideband (USB). We reduced and calibrated the data using the GILDAS pipeline at the IRAM headquarters in Grenoble. We produced uv visibility tables and performed analysis in the uv space, following the methods described in [Jin et al. \(2019, 2022, 2024\)](#). The clean continuum image was produced using the GILDAS

HOGBOM clean routine. The final data product reaches a continuum sensitivity of $33 \mu\text{Jy}$ at a central frequency of 224 GHz. The resulting synthesized beam is $1''.85 \times 1''.80$, thus the source is unresolved. We do not detect the dust continuum emission from NS_274. We, thus, place a 3σ upper limit on its observed flux density of $\mu F_{260\mu\text{m, rest}} \leq 0.1 \text{ mJy}$ (over a beam, considering that the source is unresolved). We show in Figure 1 an RGB image of NS_274⁴, where we overlay the contours of the dust continuum emission recorded with NOEMA.

RUBIES-UDS-QG-z7 falls in the footprint of the Public Release IMaging for Extragalactic Research program (PRIMER, PID 1837, PI: J. Dunlop) in the UDS field. In this case, we made use of the available JWST NIRCам and MIRI imaging (v7.2) available on DJA and covering the $0.9 - 18 \mu\text{m}$ interval. For consistency with the analysis in Weibel et al. (2024a), we adopted their total photometry, extracted in $0''.32$ diameter apertures in PSF-matched images, then corrected for aperture effects and the extinction of our Galaxy. The procedure is detailed in Weibel et al. (2024b), to which a custom extraction of the MIRI photometry in $0''.5$ diameter apertures in the F770W and F1800W images has been added. We notice that following a procedure similar to that employed for NS_274 returns fluxes $\sim 20\%$ fainter without introducing any significant color differences, thus not appreciably affecting the results of this paper.

2.2. Spectroscopy

JWST/NIRSpec Micro-Shutter Array (MSA) spectra of sources in the G165 cluster field were obtained with the PRISM/CLEAR ($0.7 - 5.3 \mu\text{m}$, $R \approx 20 - 300$), medium resolution gratings G140M/F100LP ($0.9 - 1.8 \mu\text{m}$, $R \approx 1000$), and G235M/F170LP ($1.6 - 3.2 \mu\text{m}$, $R \approx 1000$) on April 22, 2023 (PID 4666, PI: B. Frye). The science exposure times were 4420s, 6696s, and 919s for G140M/F100LP, G235M/F170LP, and the PRISM/CLEAR observations, respectively (Frye et al. 2024). NS_274 was among the targeted sources. The spectra were acquired with a 3-microshutter configuration and a 3-nod nodding pattern. Also in this case, we retrieved the spectra from the DJA (version v3). These were reduced with the MSAEXP pipeline (Brammer 2024) along the same lines detailed in Heintz et al. (2024) and de Graaff et al. (2024a). The current public version of MSAEXP includes updated reference files and improves on the absolute and color-dependent flux calibration and the bar shadow correction. The spectra were optimally extracted (Horne 1986) and their noise budget conservatively scaled up such that the residuals of a wavelength-dependent polynomial model subtracted to the spectrum are normally distributed, as expected for pure background integrations. This corresponds to a $\sim 25\%$, 25% , and 45% noise median increase for the PRISM, G140M, and G235M spectra. Finally, we anchored the spectra to the total photometry as derived in Section 2.1 to correct for residual slit losses. We applied a fourth-order polynomial correction to the spectra resulting in slowly varying rescaling of the order of 5-40%, the most extreme correction being only at the very blue end of the PRISM spectrum. The results are robust against the exact choice of the scaling function (spline, Chebyshev polynomials) and the degree of the polynomial (a simple constant or parabolic functional form already corrects for most of the offset between the spectra and the total photometry). The photometry and spectra of NS_274 are shown in Figure 2.

⁴ The image was produced with TRILogy by D. Coe, <https://github.com/dancoe/Trilogy>

NIRSpec/MSA spectra of RUBIES-UDS-QG-z7 were obtained on July 25, 2024 with PRISM/CLEAR and G395M/F290LP as part of the Red Unknowns: Bright Infrared Extragalactic Survey survey (RUBIES, PID 4233, PIs: A. de Graaff & G. Brammer). Both spectra were acquired with 2880s combined integrations with a 3-microshutter configuration and a 3-nod nodding pattern. These spectra were reduced following the same steps as detailed above. The photometry and PRISM spectrum of RUBIES-UDS-QG-z7 are shown in Figure 3. The G395M spectrum does not show any appreciable absorption features at high enough S/N (Weibel et al. 2024a), which resulted in relatively loose initial redshift constraints ($z = 7.29 \pm 0.01$).

On July 23, 2024, a G235M/F170LP spectrum was also obtained as part of the “DeepDive” survey (PID 3567, PI: F. Valentino; Ito et al. in prep.). A similar nodding pattern was used also in this case, but leaving 3 extra shutters open for an optimal background subtraction. The total integration time was of 10,590 s. The G235M/F170LP grating was processed with a customized version of MSAEXP that allowed us to recover the whole wavelength range permitted by the combination of the F170LP long-pass filter and projection on the detector (Brammer et al. in prep.). The distributed JWST pipeline automatically cuts the red end of the grating spectra to avoid contamination of the primary first spectral order with higher orders, which appear at predictable locations and intensities (Jakobsen et al. 2022). However, by extending the wavelengthrange⁵ pipeline reference file and calibrating the intensities of the second and third order spectra (which include the full response of the telescope, the shape of the filters, and flat-fielding, all summarized in a revised sensitivity curve), the full spectrum recorded on the detector can be recovered. The sensitivity curve extending beyond the nominal coverage of the filter ($1.6 - 3.2 \mu\text{m}$) was derived from the wavelength and flux commissioning and calibration programs COM PIDs 1125 (PI: J. Muzerolle Page), 1128 (PI: N. Luetzendorf) and CAL PID 1538 (PI: K. Gordon). This allowed us to extend the spectrum up to $4.2 \mu\text{m}$, now crucially covering the full Balmer break (Figure 3). The normalization and continuum shape of the extended G235M/F170LP spectrum is consistent with that of the G395M/F290LP spectrum in the overlapping regions without introducing any further corrections. Given the intrinsic red spectrum of the target and the decreasing transmission of the G235M disperser at $\lambda \gtrsim 2.3 \mu\text{m}$, the uncertainties on the flux calibration after modeling the contamination of the higher order spectra are comparable with the errors on the standard absolute calibration. In addition, the extended G235M spectrum has an approximately $1.7\times$ higher spectral resolution than G395M at a given wavelength where they overlap. Finally, to avoid spurious systematics when comparing our analysis with that of Weibel et al. (2024a), we anchored both the extended G235M and the G395M spectra to their PRISM data. In this case, the median noise rescaling amounts to 10% and 50% for the PRISM and G235M, respectively, and no appreciable difference for G395M⁶.

⁵ https://jwst-pipeline.readthedocs.io/en/latest/jwst/references_general/wavelengthrange_reffile.html

⁶ At this point, the reader might wonder about the extension of the spectra of NS_274. We briefly describe their content and limitations in Appendix A.

Table 1. Measurements and physical properties.

Property	NS_274	RUBIES-UDS-QG-z7
RA [deg]	171.82361998	34.4296173
Decl. [deg]	42.46964557	-5.1122962
z_{spec}	4.1061 ± 0.0003	7.2758 ± 0.0011
μ	2 ± 0.2	1
μ [Ne III] λ 3869 [10^{-19} cgs]	$2.4^{+2.8}_{-2.4}$	–
μ [O II] λ 3729 [10^{-19} cgs]	< 6.6	–
μ H β λ 4863 [10^{-19} cgs]	$8.1^{+3.7}_{-3.8}$	–
μ [O III] λ 5008 [10^{-19} cgs]	$8.9^{+3.9}_{-4.2}$	–
$\mu m_{\text{F200W,AB}}$	23.34 ± 0.05	26.31 ± 0.06
$\log(M_{\star}/M_{\odot})$	$10.57^{+0.02}_{-0.02}$	$10.15^{+0.05}_{-0.04}$
A_V	$0.31^{+0.03}_{-0.03}$	$0.48^{+0.07}_{-0.09}$
SFR _{100Myr} [$M_{\odot} \text{ yr}^{-1}$]	$8.4^{+0.1}_{-0.2}$	12^{+96}_{-12}
SFR _{IR, 8–1000μm} [$M_{\odot} \text{ yr}^{-1}$]	< 12	–
SFR _[OII] [$M_{\odot} \text{ yr}^{-1}$]	< 0.3	–
SFR _{Hβ} [$M_{\odot} \text{ yr}^{-1}$]	$1.2^{+0.6}_{-0.6}$	–
$\log(\text{sSFR}_{100\text{Myr}}/\text{yr}^{-1})$	$-9.64^{+0.03}_{-0.03}$	$-9.0^{+0.9}_{-3.5}$
σ_{\star} [km s ⁻¹]	255^{+39}_{-42}	–
Δv_{off} [km s ⁻¹]	-182 ± 50	-169 ± 46
R_{maj} [pc]	262^{+17}_{-15}	209^{+33}_{-24}
n_{Sersic}	$6.5^{+0.6}_{-0.5}$	$2.4^{+1.5}_{-0.9}$
$\log(M_{\text{dyn}}/M_{\odot})$	$10.18^{+0.13}_{-0.16}$	–
$\log(N(\text{FeII})/\text{cm}^{-2})$	15.00 ± 0.19	–
$\log(N(\text{MgII})/\text{cm}^{-2})$	15.35 ± 0.74	~ 17.9
$\log(N(\text{NaI})/\text{cm}^{-2})$	12.15 ± 0.59	–
$\log(N(\text{H}_{\text{Fe}})/\text{cm}^{-2})$	21.22 ± 0.19	–
$\log(N(\text{H}_{\text{Mg}})/\text{cm}^{-2})$	20.59 ± 0.74	~ 23.1
$\log(N(\text{H}_{\text{Na}})/\text{cm}^{-2})$	19.82 ± 0.59	–
\dot{M}_{out} [$M_{\odot} \text{ yr}^{-1}$] (Fe, Mg, Na)	$(5^{+5}_{-3}, 1^{+7}_{-1}, 0.2^{+0.8}_{-0.2})$	$(-, \sim 269, -)$
η (Fe, Mg, Na)	$(0.3^{+0.3}_{-0.2}, 0.1^{+0.4}_{-0.1}, 0.01^{+0.05}_{-0.01})$	$(-, \sim 42, -)$

Notes. Upper limits at 3σ . The [Ne III], [O II], H β , and [O III] fluxes refer to emission lines obtained after subtracting the underlying stellar continuum. For RUBIES-UDS-QG-z7, we report the estimate from the extended G235M spectrum.

3. Methods

3.1. Spectrophotometric modeling

3.1.1. NS_274

Initially, we re-derived the systemic redshift of NS_274 by modeling the stellar absorption features in the rest-frame optical probed by the G235M grating (Figure 2). We did so with the Penalized PiXel Fitting code (pPXF, Cappellari & Emsellem 2004) and following an approach similar to that in Cappellari (2023). We used models from the Flexible Stellar Population Synthesis library (FSPS, Conroy & Gunn 2010) normalized around the rest-frame optical V-band. We ran the code twice: we initially masked regions potentially contaminated by emission lines, then identified and excluded 3σ outlier pixels, and re-ran the modeling. We allowed only for multiplicative polynomials of 4th order as correction factors to the overall shape of the

spectrum, but this choice did not affect the robustness of the redshift solution ($z_{\text{spec}} = 4.1061 \pm 0.0003$, slightly lower, but consistent with $z = 4.1076 \pm 0.0023$ first reported in Table 2 of Frye et al. 2024) and of the stellar velocity dispersion estimate. We derive a value of $\sigma_{\star} = 255^{+39}_{-42}$ km s⁻¹ by modeling the stellar absorption features in the spectrum, excluding deep Balmer lines (H β , H γ , H δ) and other portions of the wavelength range possibly impacted by strong emission lines ([O III], [O II]). We corrected this estimate for the wavelength dependent instrumental resolution, which we assumed a factor of 1.3 \times higher than the nominal resolving power (de Graaff et al. 2024a). Finally, we attempted to add an ionized gas component typically responsible for the emission of bright rest-frame optical emission lines (e.g., Balmer lines, [O II], [O III]), but the code failed to converge on meaningful detections. We thus place upper limits on the emission lines fluxes covered by the G235M grating by assuming a line width identical to that of the stellar

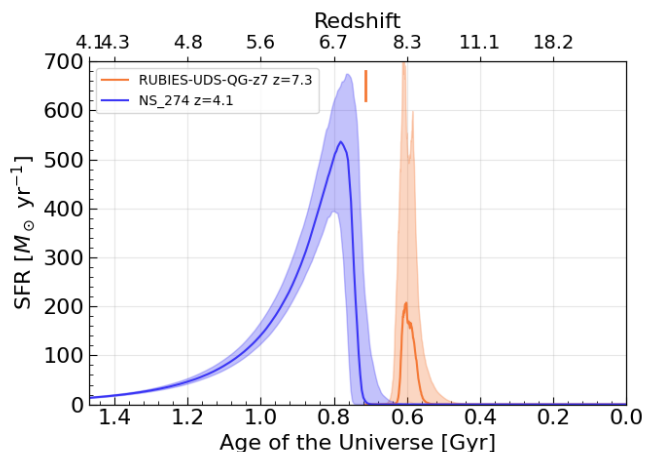


Fig. 4. Star formation histories of our targets. In orange and blue, we show the best-fit double power-law SFHs of RUBIES-UDS-QG-z7 and NS_274 and their uncertainties, respectively. The age of the Universe is truncated at the observed redshift of NS_274. The orange segment marks the observed redshift of RUBIES-UDS-QG-z7.

absorption⁷ (see Übler et al. 2024 and references therein for a recent discussion on this assumption). These values are reported in Table 1. The uncertainties are derived by bootstrapping the spectrum 500 times and repeating the modeling procedure.

Once the systemic redshift was determined, we simultaneously modeled NIRCcam and WFC3 photometry and the combined NIRSpc grating data using Bagpipes (Carnall et al. 2018, 2020). We adopted Bruzual & Charlot (2003) SPS models, the parameterization of the dust attenuation law in Salim et al. (2018) (with fixed UV bump amplitude, $B = 1$, and slope deviation from a Calzetti et al. 2000 law, $\delta = -0.2$, for a shape similar to that in Kriek & Conroy 2013), and a default Kroupa & Boily (2002) IMF. We adopted a double-power law SFH, which offers enough flexibility to capture a fast rise and decline of the SFR in the past. We fixed the value of the stellar velocity dispersion to $\sigma_* = 252 \text{ km s}^{-1}$. The adopted priors and their shapes are collected in Table B.1 and shown in Figure B.2. The fitted data and best model are shown in Figure 2, while we report best-fit parameters of interest in Table 1. A corner plot with the posterior distributions of such parameters is shown in Appendix B.1. We tested these results against the use of looser priors, different parameterizations of the SFHs (e.g., lognormal, delayed τ -models), and a different code (Fast++, Schreiber et al. 2018b). We also attempted to model the photometry, grating, and PRISM independently or combined. Finally, we explored the effect of the imposed priors on the final estimates of interesting physical quantities at test. We found the best-fit estimates to be consistent across this range of tests and robust against the choice of the priors.

Accounting for the magnification effect ($\mu = 2 \pm 0.2$), we estimate an intrinsic stellar mass of $\sim 4 \times 10^{10} M_\odot$. The SED modeling suggests that NS_274 underwent a short and intense (peak $\mu\text{SFR} \sim 500 M_\odot \text{ yr}^{-1}$) growth spurt approximately $\sim 500 \text{ Myr}$ prior to the time of observations, leaving behind some modest level of SFR over the last 100 Myr (intrinsic $\text{SFR}_{100 \text{ Myr}} \sim 8.4^{+0.1}_{-0.2} M_\odot \text{ yr}^{-1}$, Figure 4). We also constrain the dust obscured SFR by

⁷ See Appendix A for an attempt to measure emission lines in the extended G235M spectrum

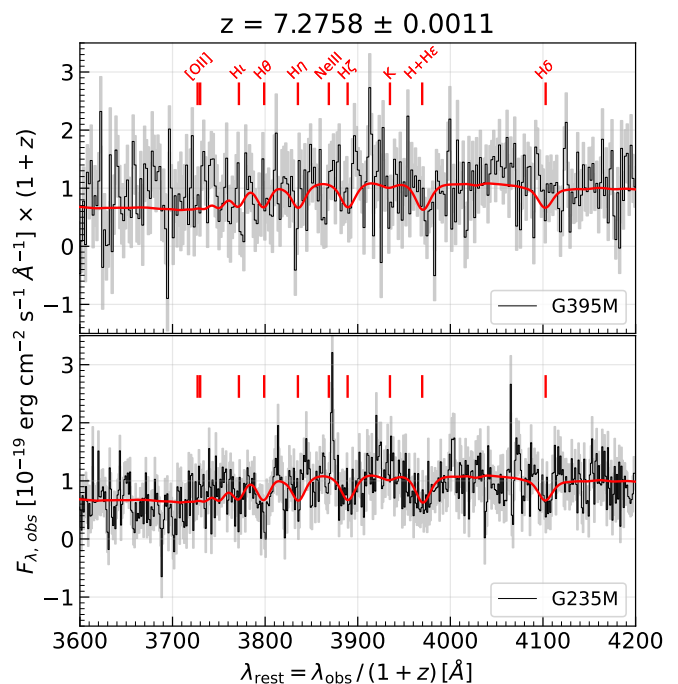


Fig. 5. Zoom into the Balmer break region of RUBIES-UDS-QG-z7 in the G395M spectrum from Weibel et al. (2024a, top) and our extended G235M spectrum (bottom). The black and gray lines show the data and their uncertainties. The red lines indicate the best-fit model (Sec. 3.1.2). The red ticks indicate the most notable absorption features as labeled.

rescaling a modified black body with dust temperature $T_{\text{dust}} = 35 \text{ K}$ and β slope of 1.8 (Witstok et al. 2023) to the upper limit on the continuum emission at $260 \mu\text{m}$ rest-frame, while accounting for the effect of the cosmic microwave background (da Cunha et al. 2013). The resulting $\text{SFR}_{\text{IR}, 8-1000 \mu\text{m}}$, using the conversion in Kennicutt (1998) adapted for our assumed IMF and corrected for the magnification factor, is of $< 12 M_\odot \text{ yr}^{-1}$ (at the 3σ level). This value is consistent with the estimate from the modeling of the shorter wavelength SED, also characterized by a low estimate of A_V . The absence of strong [O II], [O III], and $\text{H}\beta$ emission further constrains the more recent SFR on shorter timescales of 10 Myr. It also implies the absence of a bright AGN radiating efficiently (e.g., $[\text{O III}]/\text{H}\beta = 1.1^{+1.2}_{-0.5}$, but see Appendix A and Wu 2024 for caveats and limits on faint and radiatively inefficient AGN activity). Table 1 reports the constraints on SFR from the emission lines assuming the conversion in Kennicutt (1998) for $\text{H}\beta$ and Kewley et al. (2004) for [O II], correcting for the dust attenuation for the stellar continuum from the SED modeling and for the assumed IMF. These constraints place NS_274 in a post-starburst phase, as also supported by the deep stellar Balmer absorption lines. Estimates of the Lick indices ($D4000_n = 1.25 \pm 0.02$, Balogh et al. 1999; $\text{H}\gamma_A = 6.91 \pm 0.80$ and $\text{H}\delta_A = 7.83 \pm 0.75$, Worthey & Ottaviani 1997, following the procedure detailed in Gallazzi et al. 2014) are indeed typical of post-starburst systems in the local Universe.

3.1.2. RUBIES-UDS-QG-z7

The extended G235M spectrum shows absorption features that are not visible in the G395M spectrum (Figure 5). While the depth of the spectrum does not allow for a robust estimate of the stellar velocity dispersion from these lines, a collective model of their wavelengths tightly constrains the redshift. To combine the

information from both the G235M and G395M spectra at their respective resolutions, we proceeded as follows. We ran pPXF with a similar setting as for NS_274 on the extended G235M spectrum. We then took the best-fit template at its intrinsic resolution and simultaneously fitted it to both the G235M and G395M spectra, convolving the model to their corresponding resolution curves. We allowed for a normalization rescaling for each spectrum, but the shape of the template was fixed. The remaining free parameters were the redshift and the velocity dispersion. The fitting procedure was implemented using `EMCEE` (Foreman-Mackey et al. 2013), where we assumed a Gaussian likelihood and flat priors. The best-fit model is shown in Figure 5, corresponding to $z = 7.2758 \pm 0.0011$, which is consistent with the PRISM-based determination. The corner plot with the posterior distributions of the free parameters is shown in Figure B.3 in Appendix B. As noted, the velocity dispersion is poorly constrained, which is why it will not be considered any further in the analysis.

For consistency with the work by Weibel et al. (2024a), we opted for modeling the PRISM spectrum and photometry with BAGPIPES using the same set of assumptions as for our fiducial model of NS_274, but fixing the redshift to our revised estimate. The best-fit parameters (Table 1) and the overall shape of the SFHs are broadly consistent with those reported in Weibel et al. (2024a). The modeled data and the best-fit models are shown in Figure 3. Also in this case, the modeling suggests that RUBIES-UDS-QG-z7 experienced a short and vigorous main formation burst (peak SFR $\sim 200 M_{\odot} \text{ yr}^{-1}$) approximately ~ 150 Myr prior to the observed redshift, immediately followed by an abrupt suppression of the SFR ($\text{SFR}_{100\text{Myr}} = 12^{+96}_{-12} M_{\odot} \text{ yr}^{-1}$, Figure 4). As noted in the past (de Graaff et al. 2024b), the unconstrained stellar metallicity does have an impact on the reconstructed SFH and SFR estimates. In this case, the preferred solution ($Z \sim 0.5Z_{\odot}$) is in between the low- ($\sim 0.1Z_{\odot}$) and high- Z ($\sim Z_{\odot}$) models in Weibel et al. (2024a). On shorter timescales, the upper limit on the emission lines set a constraint on the SFR of $\lesssim 6 M_{\odot} \text{ yr}^{-1}$ (Weibel et al. 2024a).

3.2. Rest-frame UV and optical absorption features tracing outflowing neutral gas

A few rest-frame UV absorption lines tracing the presence of neutral gas from low-ionization elements in galaxies (Mg II doublet at $\lambda\lambda 2797, 2803$; Fe II at $\lambda\lambda 2586, 2600; 2374, 2382$) are robustly detected in the G140M spectrum of NS_274 (Figure 6). Absorption features at similar redshifts are also at least tentatively detected (e.g., Mg I at $\lambda 2853$). In the rest-frame optical covered by the G235M grating, we also robustly detect the Na I D $\lambda\lambda 5891, 5897$ doublet in absorption (although blended at this resolution), indicating an additional dense, and dusty component in the neutral gas-phase. Common to all these features is a blueshift compared to the systemic redshift derived from the well-detected stellar absorption features, indicating a substantial column of outflowing gas in the line of sight. In the case of RUBIES-UDS-QG-z7, given the limited S/N and coverage, we are only able to robustly detect the presence of Mg II (Figure 6).

3.2.1. Modeling

To explore the properties of the outflowing gas, we consistently model these absorption features with `VOIGTFIT` (Krogager 2018)⁸

⁸ <https://github.com/jkrogager/VoigtFit>

following the approach in Heintz et al. (2023). The code models the lines with Voigt profiles at the delivered spectral resolution and returns the column densities N and broadening parameters b due to thermal and turbulent motions for an arbitrary number of velocity components. Since absorption from stars and the interstellar medium (or even emission from the latter) can arise at the systemic redshift (Sugahara et al. 2017; Man et al. 2021; Davies et al. 2024), when modeling the lines in the spectra of NS_274, we implemented a two-component model, with one at fixed $z = z_{\text{spec}}$. We also ran the code iteratively: a first pass with free broadening parameters b and velocity offsets Δv_{off} to determine the latter, followed by a second iteration at fixed parameters to derive the column densities of the outflowing component. However, given the available resolving power ($R \approx 1000$) and depth, the final estimates of N are affected by significant uncertainties (Table 1). The same conditions also limit more refined modeling of stellar population in the rest-frame UV (Maltby et al. 2019), which we thus leave for future work with better data quality (but see Wu 2024 for an attempt). When simultaneously modeling the Fe, Mg, and Na transitions, we tied their broadening parameter b and velocity structure, assuming that they physically trace the bulk of the neutral gas-phase in galaxies. Considering that the ionization potentials of the elements considered here (Na 5.1 eV, Fe 7.9 eV, Mg 7.6 eV) are comparable and lower than that of hydrogen (13.6 eV), this assumption is physically motivated. Finally, we note that, in principle, $\log(N(\text{MgII}))$ might be underestimated due to saturation of the line core. Given the limited information in the spectra of RUBIES-UDS-QG-z7, we do not attempt a two-component model and fixed $b = 100 \text{ km s}^{-1}$, which is consistent with the results for NS_274. We caution the reader that this might lead to an underestimate of the velocity offset and of $\log(N)$. Deeper and higher resolution spectra will help to address several of these issues in the future.

The best-fit models obtained with `VOIGTFIT` are shown in Figure 6. We derive an average velocity offset of the absorbing gas of $\Delta v_{\text{off}} = -182 \pm 50 \text{ km s}^{-1}$ and $-169 \pm 46 \text{ km s}^{-1}$ for NS_274 and RUBIES-UDS-QG-z7, respectively, with tails extending up to a few hundred km s^{-1} . In the case of NS_274, the velocity structure is derived from the joint modeling of the Mg II, Mg I, Fe II, and Na I lines mentioned above, and the offset is consistent with the estimate first reported in Wu (2024). However, the wavelength shifts of each line are consistent. These results indicate that the dominant neutral gas column is associated with the outflowing gas. The estimated column densities are reported in Table 1. We convert $\log(N(\text{FeII}))$, $\log(N(\text{MgII}))$, and $\log(N(\text{NaI}))$ into $\log(N_{\text{H}})$, assuming a gas-phase metallicity and empirical depletion patterns, under the same assumptions detailed in Wu (2024):

$$\log(N_{\text{H}}) = \log(N_{\text{X}}) - \delta_{\text{depl}, \text{X}} - \log(N_{\text{X}}/N_{\text{H}})_{\odot} - \log(Z/Z_{\odot}), \quad (1)$$

where $X = \text{Fe, Mg, Na}$, $\delta_{\text{depl}, \text{X}}$ is the metal depletion onto dust ($\delta_{\text{Fe}} = -1.7$, $\delta_{\text{Mg}} = -0.8$ are the median values in the Galactic disk (Jenkins 2009), and $\delta_{\text{Na}} = -0.95$ is the canonical estimate for the Milky Way from Savage & Sembach 1996), $\log(N_{\text{X}}/N_{\text{H}})_{\odot}$ are the solar abundance patterns for Fe (-4.49), Mg (-4.42), and Na (-5.69, Savage & Sembach 1996), and Z the metallicity of the targets. We included a $10\times$ neutral fraction correction for Na I, but this number could be substantially higher in the extreme conditions of a recent burst of star formation or AGN activity at high redshift (Veilleux et al. 2020). We do not apply any ionization corrections for Fe and Mg, assuming that the singly ionized ions are the dominant population. This

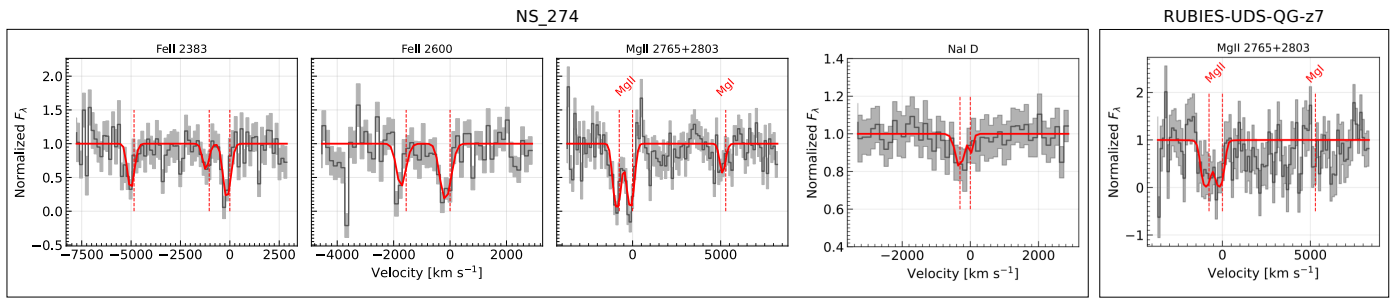


Fig. 6. Blue-shifted absorption features. The continuum-normalized spectrum (black line) and its uncertainties (gray line) around FeII, MgII+MgI, and NaID lines is shown for NS_274 at $z = 4.1$ (left panels). For RUBIES-UDS-QG-z7, we show the G235M spectrum around MgII+MgI (rightmost panel). The best-fit model with VoigtFit is marked by the solid red line. The systemic velocity for each line is marked by dashed red lines.

allows us to draw a direct comparison with the analysis in Wu (2024) without introducing major systematics. For reference, we assume $Z = Z_{\odot}$. The values from our spectrophotometric modeling are consistent with it, but they are a source of major uncertainty. This is particularly true for RUBIES-UDS-QG-z7, whose high redshift would suggest a metallicity lower than and an abundance pattern different from solar (Weibel et al. 2024a).

Finally, we note that, at this stage, the velocity offset can in principle be interpreted as due to a genuine neutral gaseous outflow or from a cloud intervening gas along the line of sight. However, this second possibility is disfavored by the absence of credible galaxies associated with the putative absorbers along the line of sight in the surrounding of our targets, although low surface brightness galaxies that fall below the flux limit cannot be ruled out.

3.3. Structural properties

Morphological properties for RUBIES-UDS-QG-z7 were derived in Weibel et al. (2024a) using the Bayesian code PYSERSIC (Pasha & Miller 2023)⁹. The authors retrieve an effective semi-major axis of $R_{\text{maj}} = 209^{+33}_{-24}$ pc for a rather round shape (axis ratio of $R_{\text{min}}/R_{\text{maj}} = 0.89^{+0.08}_{-0.14}$) and a relatively low, but poorly constrained, Sérsic (1968) index of $n = 2.4^{+1.5}_{-0.9}$. Here we follow a similar procedure and model the emission of NS_274 in the F200W band using the same code. The choice of the band is a compromise between mapping relatively long wavelengths ($\sim 4000\text{\AA}$ rest-frame) at the highest possible resolution (sampled with a $0''.02$ pixel scale) and S/N ratio. We built a PSF model by broadening the profile derived with WEBBPSF (Perrin et al. 2014) to match the width of observed unsaturated stars in the field, as described in Ito et al. (2024b). We modeled a single Sérsic (1968) profile. The source is resolved: we estimate an effective semi-major axis of $R_{\text{maj}} = 262^{+17}_{-15}$ pc and a high $n = 6.5^{+0.6}_{-0.5}$ index. We applied an average $\mu^{-0.5}$ correction to the effective size to account for the mild lensing effect. Nevertheless, this correction does not substantially alter the conclusions of this work. The source is slightly elongated (ellipticity $\epsilon = 1 - R_{\text{min}}/R_{\text{maj}} = 0.49^{+0.02}_{-0.02}$, where R_{min} is the semi-minor axis). We show the best-fit model and the residuals in Appendix B. These results are consistent with the analysis with GALFIT (Peng et al. 2002) in Wu (2024), once the lensing correction is accounted for.

Combined with the stellar velocity dispersion, we estimate the dynamical mass expected for NS_274 as:

$$M_{\text{dyn}} = K(n) K(q) \sigma_{\star}^2 R_{\text{maj}} / G, \quad (2)$$

where $K(n) = 8.87 - 0.831n + 0.0241n^2$ depends on the Sérsic index n (Cappellari et al. 2006), $K(q) = (0.87 + 0.38e^{-3.78(1-q)})^2$ depends on the projected axis ratio q (van der Wel et al. 2022), R_{maj} is the semi-major axis, and G is the gravitational constant. After accounting for the lensing effect, $\log(M_{\star}/M_{\odot}) = 10.57^{+0.02}_{-0.02}$ is higher than, but in overall agreement with $\log(M_{\text{dyn}}/M_{\odot}) = 10.18^{+0.13}_{-0.16}$, especially considering the numerous assumptions on the stellar population and dynamical modeling behind each of these calculations and the typical systematic uncertainties (Table 1).

4. Outflow properties

So far, we ascertained the presence of Mg I and Mg II, and in the case of NS_274, also Fe II and NaID blue-shifted absorption features in the spectra of two post-starburst, recently quenched galaxies at high redshift.

How much gas is outflowing from these galaxies and at what rate? Adopting the simple spherical thin-shell model in Wu (2024) and Davies et al. (2024), we derive the outflowing mass M_{out} and its rate \dot{M}_{out} as:

$$\begin{aligned} M_{\text{out}} &= 1.4 m_{\text{p}} \Omega N(\text{H}) R_{\text{out}}^2, \\ \dot{M}_{\text{out}} &= 1.4 m_{\text{p}} \Omega N(\text{H}) R_{\text{out}} v_{\text{out}}, \end{aligned} \quad (3)$$

where m_{p} is the proton mass, Ω the solid angle subtended by the outflow, R_{out} the shell radius, and v_{out} its velocity (Rupke et al. 2005). We adopt the same approach as in Wu (2024) to directly compare with their results and avoid systematics. We thus assume $\Omega = 0.45 \times 4\pi$ (based on Davies et al. 2024), $R_{\text{out}} = 2R_{\text{maj}}$, and $v_{\text{out}} = \Delta v_{\text{off}}$ is the average outflow velocity from our fit (Table 1). For NS_274, we obtain $\log(M_{\text{out}}/M_{\odot}) = 7.5^{+0.2}_{-0.2}$, $6.9^{+0.7}_{-0.7}$, and $6.1^{+0.6}_{-0.6}$ from Fe, Mg, and Na respectively. The estimate based on Fe is in good agreement with that reported in Wu (2024) ($\log(M_{\text{out}}/M_{\odot}) \sim 7.8$), while that derived from Mg is $\sim 10\times$ larger. The outflow mass from Fe and Mg are in agreement, while that from Na is lower by ~ 1 dex at face value. This might be due to the fact that the observed transitions, while broadly tracing the neutral hydrogen phase of the ISM, are sensitive to gas conditions, with NaI D preferentially being a proxy of the colder and denser gas. For RUBIES-UDS-QG-z7, we derive $\log(M_{\text{out}}/M_{\odot}) \sim 9.1$ from Mg, based on a column density of

⁹ <https://github.com/pysersic/pysersic>

$\log(N(\text{MgII})/\text{cm}^{-2}) \sim 17.9$. These estimates are more uncertain than those derived for NS_274 (largely due to the assumption on b , the absence of S/N to constrain Fe lines, and a systemic component) and their face values should be taken with a grain of salt. The derived HI column density is remarkably high (Table 1) and, if confirmed, its effects could be tested in deeper PRISM data around the Lyman limit (e.g., Heintz et al. 2024).

We estimate mass outflow rates of $\dot{M}_{\text{out}} \sim 0.2 - 5 M_{\odot} \text{ yr}^{-1}$ and $\sim 269 M_{\odot} \text{ yr}^{-1}$ for NS_274 and RUBIES-UDS-QG-z7, respectively. The range in \dot{M}_{out} for NS_274 reflects the difference in $\log(N(\text{H}))$ from Na and Fe. The high column density from Mg dominates this high, albeit uncertain, estimate of \dot{M}_{out} for RUBIES-UDS-QG-z7. The corresponding mass loading factors are $\eta = \dot{M}_{\text{out}}/\text{SFR} \sim 0.01 - 0.3$ and ~ 42 for NS_274 and RUBIES-UDS-QG-z7, where we adopted the SFR averaged over the last 100 Myr for the calculation.

5. Discussion

5.1. Outflow velocities in recently quenched galaxies across time

In Figure 7, we show the average outflow velocities v_{out} as a function of M_{\star} , SFR, and SFR surface density ($\Sigma_{\text{SFR}} = \text{SFR}/(2\pi R_{\text{eff}}^2)$) for samples of star-forming and post-starburst galaxies up to $z \sim 1.5 - 2$ based on the large literature compilation in Davis et al. (2023). In this case, we considered outflows predominantly traced by Mg and Fe absorption to minimize the systematics in the comparison. Interestingly, in terms of average outflow velocities, the neutral gas outflows in NS_274 and RUBIES-UDS-QG-z7 are broadly consistent with those observed in local star-forming and post-starburst galaxies at fixed M_{\star} , SFR, or Σ_{SFR} . The velocity offsets measured in two lensed recently quenched systems at $z \sim 3$ in Man et al. (2021) and in the stacked spectra of post-starburst galaxies at $1 < z < 1.4$ in Maltby et al. (2019) are also shown for reference. In both cases, they are also consistent with the correlations observed at lower redshifts.

The fact that the average velocities detected in NS_274 and RUBIES-UDS-QG-z7 at high redshift are overall consistent with those observed in nearby post-starburst galaxies seems to suggest that the mechanisms launching them during or shortly after quenching are similar to those operating in the local Universe. This is best captured in the tightest among the correlations, the one between v_{out} and Σ_{SFR} (Heckman et al. 2015). In this case, the typically higher SFRs at fixed stellar masses at high redshift are balanced by an increasing compactness, so that the launch of winds via copious star formation occurring in small volumes, as one could expect to detect in early galaxies immediately after quenching, is consistent with that observed in rarer, similarly massive systems at low redshift. However, only larger samples of recently quenched galaxies at $z > 2 - 3$ will tell us if this is the case, or if a bona fide evolution of the $v_{\text{out}} - \Sigma_{\text{SFR}}$ (and M_{\star} , SFR) relations exists (Sugahara et al. 2017).

We also note that the scaling relations considered here do not include any explicit terms to account for possible AGN activity. Interestingly, samples specifically selected or consistent with post-starburst galaxies shown in Figure 7 do not show evident signs of ongoing powerful AGN activity (Maltby et al. 2019; Davis et al. 2023; the sources in Man et al. 2021 may host faint Type II AGN based on their [O III]/[O II] ratios). According to our analysis, this is the case also for the galaxies analyzed here (but see Appendix A and Wu 2024). Taken together,

this suggests that ongoing AGN activity is not necessarily required to explain the average outflow velocities of NS_274, RUBIES-UDS-QG-z7, but also lower-redshift post-starburst galaxies in Figure 7 at fixed M_{\star} , SFR, or Σ_{SFR} .

5.2. Outflow masses, loading factors, energetics

If the outflows in NS_274 and RUBIES-UDS-QG-z7 show velocities similar to those observed in more local post-starburst systems at fixed M_{\star} , SFR and Σ_{SFR} without invoking any strong AGN contribution, the simple calculations in Section 4 depict a partially different scenario, at least for RUBIES-UDS-QG-z7.

5.3. Outflows as relics of the star formation process winding down in NS_274

For NS_274, we find that the mass loading factor $\eta = \dot{M}_{\text{out}}/\text{SFR} = 0.01 - 0.3$ and the energy associated with the outflow ($\dot{E}_{\text{out}} = 0.5\dot{M}_{\text{out}}v_{\text{out}}^2 \sim 0.2 - 5 \times 10^{40} \text{ erg s}^{-1}$) are consistent with basic expectations for SNe-powered outflows, where the minimum and maximum values of these ranges are derived from the estimates of $N(\text{NaI})$ and $N(\text{FeII})$, respectively (Table 1). To show this, we adopt the approach in Veilleux et al. (2005). Based on the Starburst99 (Leitherer et al. 1999) models with solar metallicity and a Salpeter (1955) IMF, we expect an injection of energy due to SNe of the order of $\dot{E}_{\text{SN}} = 7 \times 10^{41} \times \text{SFR}_{100\text{Myr}} = (5.9 \pm 0.1) \times 10^{42} \text{ erg s}^{-1}$ and a mass outflow rate $\dot{M}_{\text{SN}} = 0.26 \times \text{SFR}_{100\text{Myr}} = (2.2 \pm 0.1) M_{\odot} \text{ yr}^{-1}$. Even neglecting a simple linear scaling to match the IMF of our choice and assuming coupling with the ISM of the order of $\sim 10\%$ or less, the injected energy is broadly consistent with our empirical estimate for NS_274. Similarly, the mass outflow rate is in agreement with our observational estimate ($\dot{M}_{\text{out}} = 0.2 - 5 M_{\odot} \text{ yr}^{-1}$, Table 1). Taken with the findings described in the previous Section, it seems that the levels of star formation over the last ~ 100 Myr is sufficient to explain the outflows observed in NS_274 (Figure 4). However, given the slow average outflow velocity ($\Delta v_{\text{off}} \sim 180 \text{ km s}^{-1}$, lower than the stellar velocity dispersion ($\sigma_{\star} \sim 250 \text{ km s}^{-1}$), and the mass loading factor $\eta \lesssim 1$, it is unlikely that the observed outflows are responsible for the quenching of star formation in NS_274.

5.4. Extreme outflow properties might indicate undetected AGN activity in RUBIES-UDS-QG-z7

The very large value of $\eta > 10$ and $\dot{E}_{\text{out}} \sim 2 \times 10^{42} \text{ erg s}^{-1}$ for RUBIES-UDS-QG-z7 give leeway to different interpretations. The mass outflow rate from Mg II ($\dot{M}_{\text{out}} \sim 269 M_{\odot} \text{ yr}^{-1}$) largely exceeds the value expected from SNe-driven winds ($\dot{M}_{\text{SN}} = 3_{-3}^{+25} M_{\odot} \text{ yr}^{-1}$), suggesting a contribution from other ejective mechanism, i.e. powered by an AGN. However, the injected energy is broadly consistent with $\dot{E}_{\text{SN}} = 8_{-8}^{+67} \times 10^{42} \text{ erg s}^{-1}$ even considering a 10% coupling with the ISM. The agreement is largely due to the loose constraints on the recent SFR estimate. The findings for RUBIES-UDS-QG-z7 are, thus, somewhat more consistent with those obtained from mapping the neutral gas outflows using the sodium NaI D tracer in recently quenched galaxies at $z = 2 - 3$, carrying large amount of gas masses and energies away from galaxies (Belli et al. 2024; Davies et al. 2024), as simulations and models postulate, despite the absence of clear ongoing AGN activity.

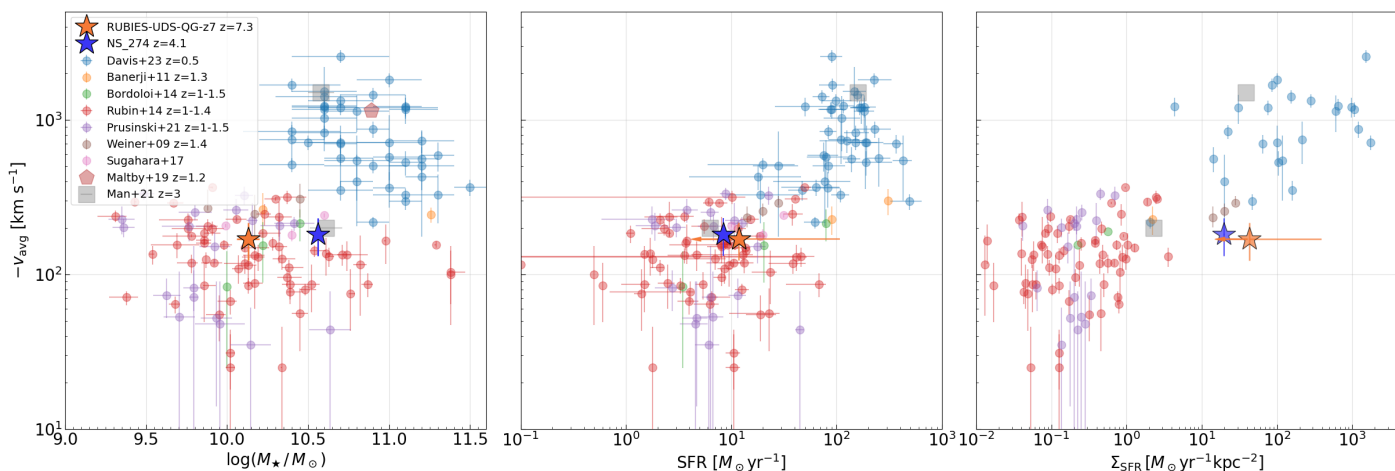


Fig. 7. Average outflow velocity as a function of the stellar mass, $\text{SFR}_{100\text{Myr}}$, and surface density of $\text{SFR}_{100\text{Myr}}$ (corrected by the magnification factor for NS_274). Filled stars indicate the targets analyzed in this work. The colored filled circles represent the homogenized literature compilation of Mg II outflows across redshifts by (Davis et al. 2023, and references therein). The results from stacking of post-starburst galaxies at $z \sim 1.2$ from Maltby et al. (2019) are shown with a red pentagon. The location of two $z \sim 3$ recently quenched sources in Man et al. (2021) is marked by grey squares.

5.5. Caveats and future perspectives

Combined with recent findings on outflows and galaxy quenching in the literature, our results for NS_274 and RUBIES-UDS-QG-z7 contribute to describing this phenomenon as being as rich and complex as it is in the local Universe, despite the much shorter time-frame in which it can occur. However, a few words of caution are due.

First, we stress that the measurements and simple calculations in the previous sections are affected by significant uncertainties and rely on several assumptions. As an example, in the case of NS_274, the mass loading factor derived in this work significantly differs from the range presented in Wu (2024) ($\eta \sim 7 - 30$), which drives us to different conclusions about the origin of the observed outflows. The disparity is mainly ascribable to the SFR estimate assumed to compute η rather than truly different values of the quantities at play. While Wu (2024) adopts SFRs averaged over 10 Myr, here we considered a 100 Myr period, a timescale on the lower end of the lifespan of outflows in the galaxy halos as suggested by observational and theoretical studies (Davis et al. 2023, and references therein). This choice also allowed us to directly compare our findings with those in the literature compilation shown in Figure 7. Together with the analysis of the origin of possible faint emission lines in the optical rest-frame spectrum, this is where our analysis of NS_274 mainly differs from that presented in Wu (2024) (see also Appendix A).

Second, definitive proof of the effect of feedback of AGN and stellar feedback on their hosts remains hard to constrain even with exquisite data and under consistent assumptions, given the widely different spatial and temporal scales of several competing processes involved. In particular, extreme outflow properties (e.g., velocities, masses, energies) can be somewhat more confidently associated with the action of AGN than to SNe, even in absence of typical signatures such as high optical line ratios or broad lines in their spectra, as in the case of RUBIES-UDS-QG-z7. This is because of the short-term AGN variability (i.e., the imprint of an AGN on outflows can outlast its presence and detectability in recently quenched galaxies) and the fact that the feedback mode that quenches star-formation in

galaxies can be characterized by low Eddington ratios in some models (Lagos et al. 2024, even if this is still matter of debate Choi et al. 2017; De Lucia et al. 2024, Farcy et al. in prep.). The variability and radiative inefficiency play also a role in the case of less extreme outflows conditions, such as those we reconstructed for NS_274 and similarly found in normal star-forming galaxies. While in principle consistent with the energy, momentum, and mass provided by SNe feedback, low values of these quantities do not exclude a significant contribution from AGN a priori, especially for galaxy-scale outflows and for those models where gas entrainment in the circumgalactic medium plays a major role (Mitchell et al. 2020).

Promising approaches to counter the effect of the short-term AGN variability rely on proxies of the integrated, rather than instantaneous, effect of the growth of supermassive black holes (e.g., their masses, Bluck et al. 2023) on their host galaxies. Valid attempts tested in the local Universe (e.g., Wang et al. 2024) are now extended to high-redshift samples (see discussion in Ito et al. 2024a; Baker et al. 2024; Onoue et al. 2024). Tying these properties with those of outflows in larger samples of galaxies similar to those presented here will be key to attenuate the effect of different spatial and temporal scales, and to obtain a more decisive evidence of how stellar and black hole masses grow and co-evolve from star-forming to quiescent phases.

6. Conclusions

In this work, we reported the detection of signatures of outflowing gas in the rest-UV and optical JWST/NIRSpec spectra of two massive ($M_\star \sim 10^{10.2} M_\odot$) and recently quenched galaxies: NS_274 at $z = 4.1601$ and RUBIES-UDS-QG-z7 at $z = 7.2758$. In particular, new observations with the G235M grating, reduced with a customized version of the MSAEXP pipeline, allowed us to ascertain the redshift of RUBIES-UDS-QG-z7, previously constrained only by low-resolution PRISM data. The presence of gas outflows is revealed by blue-shifted ionized magnesium, iron, and neutral sodium absorption features, which trace the neutral hydrogen phase. The combined analysis and spectra of these galaxies allowed us to reach the following conclusions.

- Both targets show signatures typical of recently quenched star formation. In fact, the absence of strong emission lines and the reconstructed star formation histories from spectrophotometric modeling predict low SFRs on short (10 Myr) and intermediate (100 Myr) scales ($\text{SFR}_{100\text{Myr}} \sim 15 M_{\odot} \text{yr}^{-1}$). The quiescence of NS_274 is further confirmed by the lack of strong dust continuum emission, setting an upper limit on the obscured SFR at $< 12 M_{\odot} \text{yr}^{-1}$.
- The measured outflow velocities ($\sim 180 \text{ km s}^{-1}$) are consistent with those measured in nearby ($z \lesssim 0.7$) and a few $z \sim 1 - 3$ post-starburst galaxies at fixed M_{\star} , SFR, and Σ_{SFR} without strong signatures of ongoing AGN activity. This suggests that outflows in galaxies quenched on short timescales are powered by similar mechanisms across cosmic time. This can be tested by tracing these scaling relations at $z \gtrsim 2 - 3$ (in particular, the tightest one: $v_{\text{out}} - \Sigma_{\text{SFR}}$) with large spectroscopic samples of recently quenched systems.
- Under simple assumptions, we derive outflow masses, rates, loading factors, and energetics for both galaxies – finding them to be rather different. For NS_274 at $z = 4.1$, benefiting from higher quality spectra, we find values in principle entirely consistent with predictions for SNe-powered outflows over a timescale of 100 Myr. However, low values of the mass loading factor ($\eta \lesssim 1$) and velocities indicate that it is unlikely that the observed outflows are responsible for the star formation quenching.
- For RUBIES-UDS-QG-z7, the extreme mass loading factor ($\eta \sim 50$) suggests the contribution of an undetected AGN as a powering mechanism for the observed outflow. Interestingly, this is not reflected on an extremely large average outflow velocity, which is consistent with that recorded for the outflow in NS_274 and in local post-starburst galaxies of similar M_{\star} , SFR, or Σ_{SFR} .
- Maybe more importantly, these case studies prove that it is possible to detect neutral outflowing gas in distant ($z > 4$) post-starburst galaxies via Mg and Fe in the rest-frame UV, and Na in the optical even with relatively inexpensive integrations of a handful of hours with medium resolution gratings with JWST/NIRSpec. The construction of larger samples to test scaling relations as a function of cosmic time and the comparison of outflow properties with the model predictions for SNe and AGN instantaneous and integrated feedback is the logical next step to remedy the effect of the wide range of spatial and temporal scales involved in galaxy quenching.

Acknowledgements. FV warmly thanks Christy Tremonti for providing the measurements for the literature sample shown in Figure 7. FV is also indebted to Carlos Gómez-Guijarro, the co-principal investigator of the NOEMA program, for many years of stimulating and fruitful scientific discussions on the topics presented in this work – and for his valued friendship. This work is based on observations carried out under projects number W23CU with the IRAM Interferometer NOEMA. IRAM is supported by INSU/CNRS (France), MPG (Germany) and IGN (Spain). We are grateful for the help received from IRAM staff during observations and data reduction. FV is grateful for the support of the Japanese Society for the Promotion of Science through the Fellowship (JSPS) S23108 and for the hospitality of Masayuki Tanaka and his group at the National Observatory of Japan, where part of this work has been conducted. Some of the data products presented herein were retrieved from the Dawn JWST Archive (DJA). DJA is an initiative of the Cosmic Dawn Center, which is funded by the Danish National Research Foundation under grant DNR140. FV, KI, and PZ acknowledge support from the Independent Research Fund Denmark (DFF) under grant 3120-00043B. SJ and GEM acknowledges the Villum Fonden research grants 37440 and 13160. This study was also supported by JSPS KAKENHI Grant Numbers JP22J00495 and JP23K13141, by Swiss State Secretariat for Education, Research and Innovation (SERI) under contract number MB22.00072.

References

- Antwi-Danso, J., Papovich, C., Esdaile, J., et al. 2023, arXiv e-prints, arXiv:2307.09590
- Antwi-Danso, J., Papovich, C., Esdaile, J., et al. 2025, ApJ, 978, 90
- Baker, W. M., Lim, S., D'Eugenio, F., et al. 2024, arXiv e-prints, arXiv:2410.14773
- Baldwin, J. A., Phillips, M. M., & Terlevich, R. 1981, PASP, 93, 5
- Balogh, M. L., Morris, S. L., Yee, H. K. C., Carlberg, R. G., & Ellingson, E. 1999, ApJ, 527, 54
- Barbary, K. 2016, The Journal of Open Source Software, 1, 58
- Baron, D., Netzer, H., Davies, R. I., & Xavier Prochaska, J. 2020, MNRAS, 494, 5396
- Baron, D., Netzer, H., Lutz, D., Prochaska, J. X., & Davies, R. I. 2022, MNRAS, 509, 4457
- Belli, S., Park, M., Davies, R. L., et al. 2024, Nature, 630, 54
- Bertin, E. & Arnouts, S. 1996, A&AS, 117, 393
- Bluck, A. F. L., Piotrowska, J. M., & Maiolino, R. 2023, ApJ, 944, 108
- Brammer, G. 2023, grizli
- Brammer, G. 2024, msaexp: NIRSpec analysis tools
- Bruzual, G. & Charlot, S. 2003, MNRAS, 344, 1000
- Cañameras, R., Nesvadba, N. P. H., Limousin, M., et al. 2018, A&A, 620, A60
- Calzetti, D., Armus, L., Bohlin, R. C., et al. 2000, ApJ, 533, 682
- Cappellari, M. 2023, MNRAS, 526, 3273
- Cappellari, M., Bacon, R., Bureau, M., et al. 2006, MNRAS, 366, 1126
- Cappellari, M. & Emsellem, E. 2004, PASP, 116, 138
- Carnall, A. C., Cullen, F., McLure, R. J., et al. 2024, arXiv e-prints, arXiv:2405.02242
- Carnall, A. C., McLure, R. J., Dunlop, J. S., & Davé, R. 2018, MNRAS, 480, 4379
- Carnall, A. C., McLure, R. J., Dunlop, J. S., et al. 2023, Nature, 619, 716
- Carnall, A. C., Walker, S., McLure, R. J., et al. 2020, MNRAS, 496, 695
- Choi, E., Ostriker, J. P., Naab, T., et al. 2017, ApJ, 844, 31
- Coil, A. L., Weiner, B. J., Holz, D. E., et al. 2011, ApJ, 743, 46
- Conroy, C. & Gunn, J. E. 2010, ApJ, 712, 833
- da Cunha, E., Groves, B., Walter, F., et al. 2013, ApJ, 766, 13
- Davies, R. L., Belli, S., Park, M., et al. 2024, MNRAS, 528, 4976
- Davis, J. D., Tremonti, C. A., Swiggum, C. N., et al. 2023, ApJ, 951, 105
- de Graaff, A., Brammer, G., Weibel, A., et al. 2024a, arXiv e-prints, arXiv:2409.05948
- de Graaff, A., Setton, D. J., Brammer, G., et al. 2024b, arXiv e-prints, arXiv:2404.05683
- De Lucia, G., Fontanot, F., Xie, L., & Hirschmann, M. 2024, A&A, 687, A68
- D'Eugenio, C., Daddi, E., Gobat, R., et al. 2020, ApJ, 892, L2
- D'Eugenio, F., Perez-Gonzalez, P., Maiolino, R., et al. 2023, arXiv e-prints, arXiv:2308.06317
- Foreman-Mackey, D., Hogg, D. W., Lang, D., & Goodman, J. 2013, PASP, 125, 306
- Forrest, B., Annunziatella, M., Wilson, G., et al. 2020a, ApJ, 890, L1
- Forrest, B., Marsan, Z. C., Annunziatella, M., et al. 2020b, ApJ, 903, 47
- Forrest, B., Wilson, G., Muzzin, A., et al. 2022, ApJ, 938, 109
- Förster Schreiber, N. M. & Wuyts, S. 2020, ARA&A, 58, 661
- Frye, B., Broadhurst, T., & Benítez, N. 2002, ApJ, 568, 558
- Frye, B. L., Pascale, M., Pierel, J., et al. 2024, ApJ, 961, 171
- Frye, B. L., Pascale, M., Qin, Y., et al. 2019, ApJ, 871, 51
- Gallazzi, A., Bell, E. F., Zibetti, S., Brinchmann, J., & Kelson, D. D. 2014, ApJ, 788, 72
- Glazebrook, K., Nanayakkara, T., Schreiber, C., et al. 2024, Nature, 628, 277
- Glazebrook, K., Schreiber, C., Labbé, I., et al. 2017, Nature, 544, 71
- Heckman, T. M., Alexandroff, R. M., Borthakur, S., Overzier, R., & Leitherer, C. 2015, ApJ, 809, 147
- Heintz, K. E., Brammer, G. B., Watson, D., et al. 2024, arXiv e-prints, arXiv:2404.02211
- Heintz, K. E., De Cia, A., Thöne, C. C., et al. 2023, A&A, 679, A91
- Horne, K. 1986, PASP, 98, 609
- Ito, K., Tanaka, T. S., Shimasaku, K., et al. 2024a, arXiv e-prints, arXiv:2408.08492
- Ito, K., Valentino, F., Brammer, G., et al. 2024b, ApJ, 964, 192
- Jakobsen, P., Ferruit, P., Alves de Oliveira, C., et al. 2022, A&A, 661, A80
- Jenkins, E. B. 2009, ApJ, 700, 1299
- Ji, Z., Williams, C. C., Rieke, G. H., et al. 2024, arXiv e-prints, arXiv:2409.17233
- Jin, S., Daddi, E., Magdis, G. E., et al. 2019, ApJ, 887, 144
- Jin, S., Daddi, E., Magdis, G. E., et al. 2022, A&A, 665, A3
- Jin, S., Sillassen, N. B., Hodge, J., et al. 2024, A&A, 690, L16
- Kakimoto, T., Tanaka, M., Onodera, M., et al. 2024, ApJ, 963, 49
- Kamieneski, P. S., Frye, B. L., Windhorst, R. A., et al. 2024, ApJ, 973, 25
- Kennicutt, Jr., R. C. 1998, ARA&A, 36, 189
- Kewley, L. J., Dopita, M. A., Leitherer, C., et al. 2013, ApJ, 774, 100
- Kewley, L. J., Geller, M. J., & Jansen, R. A. 2004, AJ, 127, 2002

- Kokorev, V., Chisholm, J., Endsley, R., et al. 2024, arXiv e-prints, arXiv:2407.20320
- Kriek, M. & Conroy, C. 2013, *ApJ*, 775, L16
- Krogager, J.-K. 2018, arXiv e-prints, arXiv:1803.01187
- Kron, R. G. 1980, *ApJS*, 43, 305
- Kroupa, P. & Boily, C. M. 2002, *MNRAS*, 336, 1188
- Kubo, M., Umehata, H., Matsuda, Y., et al. 2022, *ApJ*, 935, 89
- Kurinchi-Vendhan, S., Farcy, M., Hirschmann, M., & Valentino, F. 2024, *MNRAS*, 534, 3974
- Lagos, C. d. P., Valentino, F., Wright, R. J., et al. 2024, arXiv e-prints, arXiv:2409.16916
- Leitherer, C., Schaerer, D., Goldader, J. D., et al. 1999, *ApJS*, 123, 3
- Maltby, D. T., Almaini, O., McLure, R. J., et al. 2019, *MNRAS*, 489, 1139
- Man, A. W. S., Zabl, J., Brammer, G. B., et al. 2021, *ApJ*, 919, 20
- Merlin, E., Fortuni, F., Torelli, M., et al. 2019, *MNRAS*, 2241
- Mingozzi, M., James, B. L., Arellano-Córdova, K. Z., et al. 2022, *ApJ*, 939, 110
- Mitchell, P. D., Schaye, J., Bower, R. G., & Crain, R. A. 2020, *MNRAS*, 494, 3971
- Naab, T. & Ostriker, J. P. 2017, *ARA&A*, 55, 59
- Nanayakkara, T., Glazebrook, K., Jacobs, C., et al. 2024, *Scientific Reports*, 14, 3724
- Onoue, M., Ding, X., Silverman, J. D., et al. 2024, arXiv e-prints, arXiv:2409.07113
- Pascale, M., Frye, B. L., Dai, L., et al. 2022, *ApJ*, 932, 85
- Pasha, I. & Miller, T. B. 2023, *The Journal of Open Source Software*, 8, 5703
- Peng, C. Y., Ho, L. C., Impey, C. D., & Rix, H.-W. 2002, *AJ*, 124, 266
- Perrin, M. D., Sivaramakrishnan, A., Lajoie, C.-P., et al. 2014, in *Society of Photo-Optical Instrumentation Engineers (SPIE) Conference Series*, Vol. 9143, *Space Telescopes and Instrumentation 2014: Optical, Infrared, and Millimeter Wave*, ed. J. Oschmann, Jacobus M., M. Clampin, G. G. Fazio, & H. A. MacEwen, 91433X
- Rieke, M. J., Kelly, D. M., Misselt, K., et al. 2023, *PASP*, 135, 028001
- Rubin, K. H. R., Prochaska, J. X., Koo, D. C., et al. 2014, *ApJ*, 794, 156
- Rupke, D. S., Veilleux, S., & Sanders, D. B. 2005, *ApJS*, 160, 87
- Salim, S., Boquien, M., & Lee, J. C. 2018, *ApJ*, 859, 11
- Salpeter, E. E. 1955, *ApJ*, 121, 161
- Savage, B. D. & Sembach, K. R. 1996, *ARA&A*, 34, 279
- Schlafly, E. F. & Finkbeiner, D. P. 2011, *ApJ*, 737, 103
- Schreiber, C., Glazebrook, K., Nanayakkara, T., et al. 2018a, *A&A*, 618, A85
- Schreiber, C., Labbé, I., Glazebrook, K., et al. 2018b, *A&A*, 611, A22
- Sersic, J. L. 1968, *Atlas de Galaxias Australes*
- Shapley, A. E., Steidel, C. C., Pettini, M., & Adelberger, K. L. 2003, *ApJ*, 588, 65
- Somerville, R. S. & Davé, R. 2015, *ARA&A*, 53, 51
- Sugahara, Y., Ouchi, M., Lin, L., et al. 2017, *ApJ*, 850, 51
- Tanaka, M., Onodera, M., Shimakawa, R., et al. 2024, *ApJ*, 970, 59
- Tanaka, M., Valentino, F., Toft, S., et al. 2019, *ApJ*, 885, L34
- Taylor, E., Maltby, D., Almaini, O., et al. 2024, *MNRAS*, 535, 1684
- Tremonti, C. A., Moustakas, J., & Diamond-Stanic, A. M. 2007, *ApJ*, 663, L77
- Übler, H., Förster Schreiber, N. M., van der Wel, A., et al. 2024, *MNRAS*, 527, 9206
- Urbano Stawinski, S. M., Cooper, M. C., Forrest, B., et al. 2024, *The Open Journal of Astrophysics*, 7, 46
- Valentino, F., Brammer, G., Gould, K. M. L., et al. 2023, *ApJ*, 947, 20
- Valentino, F., Tanaka, M., Davidzon, I., et al. 2020, *ApJ*, 889, 93
- van der Wel, A., van Houdt, J., Bezanson, R., et al. 2022, *ApJ*, 936, 9
- Veilleux, S., Cecil, G., & Bland-Hawthorn, J. 2005, *ARA&A*, 43, 769
- Veilleux, S., Maiolino, R., Bolatto, A. D., & Aalto, S. 2020, *A&A Rev.*, 28, 2
- Wang, T., Xu, K., Wu, Y., et al. 2024, *Nature*, 632, 1009
- Weibel, A., de Graaff, A., Setton, D. J., et al. 2024a, arXiv e-prints, arXiv:2409.03829
- Weibel, A., Oesch, P. A., Barrufet, L., et al. 2024b, arXiv e-prints, arXiv:2403.08872
- Weiner, B. J., Coil, A. L., Prochaska, J. X., et al. 2009, *ApJ*, 692, 187
- Witstok, J., Jones, G. C., Maiolino, R., Smit, R., & Schneider, R. 2023, *MNRAS*, 523, 3119
- Worthey, G. & Ottaviani, D. L. 1997, *ApJS*, 111, 377
- Wu, P.-F. 2024, arXiv e-prints, arXiv:2409.00471
- Xu, X., Heckman, T., Henry, A., et al. 2022, *ApJ*, 933, 222
- ⁵ Department of Astronomy, University of Geneva, Chemin Pegasi 51, 1290 Versoix, Switzerland
- ⁶ Department of Astronomy, School of Science, The University of Tokyo, 7-3-1, Hongo, Bunkyo-ku, Tokyo, 113-0033, Japan
- ⁷ Department of Astronomy, The University of Texas at Austin, Austin, TX 78712, USA
- ⁸ Department of Astronomy, University of Massachusetts, Amherst, MA 01003, USA
- ⁹ INAF - Osservatorio Astrofisico di Arcetri, Largo Enrico Fermi 5, 50125 Firenze, Italy
- ¹⁰ Max-Planck-Institut für Astronomie, Königstuhl 17, D-69117, Heidelberg, Germany
- ¹¹ Department of Astronomy/Steward Observatory, University of Arizona, 933 N Cherry Ave., Tucson, AZ 85721-0009, USA
- ¹² School of Earth and Space Exploration, Arizona State University, PO Box 876004, Tempe, AZ 85287-6004, USA
- ¹³ Departamento de Física Teórica, Modulo 8, Facultad de Ciencias, Universidad Autónoma de Madrid, 28049 Madrid, Spain
- ¹⁴ CIAFF, Facultad de Ciencias, Universidad Autónoma de Madrid, 28049 Madrid, Spain
- ¹⁵ Caltech/IPAC, MS 314-6, 1200 E. California Blvd. Pasadena, CA 91125, USA
- ¹⁶ École Polytechnique Fédérale de Lausanne (EPFL), Observatoire de Sauverny, Chemin Pegasi 51, CH-1290 Versoix, Switzerland
- ¹⁷ Joint ALMA Observatory, Alonso de Córdova 3107, Vitacura, Casilla 19001, Santiago de Chile, Chile
- ¹⁸ National Astronomical Observatory of Japan, Los Abedules 3085 Oficina 701, Vitacura 763 0414, Santiago, Chile
- ¹⁹ European Southern Observatory, Alonso de Córdova 3107, Vitacura, Casilla 19001, Santiago de Chile, Chile
- ²⁰ Universidad Diego Portales, Av. Ejército Santiago de Chile, Chile
- ²¹ INAF – Astronomical Observatory of Trieste, Via G. B. Tiepolo 11, 34143 Trieste, Italy
- ²² Department of Astrophysical Sciences, Princeton University, Princeton, NJ 08544, USA
- ²³ Department of Astronomical Science, The Graduate University for Advanced Studies, SOKENDAI, 2-21-1 Osawa, Mitaka, Tokyo 181-8588, Japan
- ²⁴ National Astronomical Observatory of Japan, 2-21-1 Osawa, Mitaka, Tokyo 181-8588, Japan
- ²⁵ Astronomical Institute, Tohoku University, Aoba-ku, Sendai 980-8578, Japan
- ²⁶ International Centre for Radio Astronomy Research (ICRAR), M468, University of Western Australia, 35 Stirling Hwy, Crawley, WA 6009, Australia
- ²⁷ ARC Centre of Excellence for All Sky Astrophysics in 3 Dimensions (ASTRO 3D)
- ²⁸ Department of Physics & Astronomy, University of British Columbia, 6224 Agricultural Road, Vancouver BC, V6T 1Z1, Canada
- ²⁹ Subaru Telescope, National Astronomical Observatory of Japan, National Institutes of Natural Sciences (NINS), 650 North A'ohoku Place, Hilo, HI 96720, USA
- ³⁰ Kapteyn Astronomical Institute, University of Groningen, Landleven 12, 9747 AD, Groningen, The Netherlands
- ³¹ Waseda Institute for Advanced Study (WIAS), Waseda University, 1-21-1 Nishi-Waseda, Shinjuku, Tokyo 169-0051, Japan
- ³² Center for Interdisciplinary Exploration and Research in Astrophysics (CIERA), Northwestern University, 1800 Sherman Ave, Evanston, IL 60201, USA
- ³³ Institute of Astrophysics, National Taiwan University, Taipei 10617, Taiwan

¹ Cosmic Dawn Center (DAWN), Denmark

² DTU Space, Technical University of Denmark, Elektrovej 327, DK-2800 Kgs. Lyngby, Denmark

³ European Southern Observatory, Karl-Schwarzschild-Str. 2, 85748 Garching, Germany

⁴ Niels Bohr Institute, University of Copenhagen, Jagtvej 128, 2200, Copenhagen N, Denmark

Table B.1. Free parameters and priors for the spectrophotometric modeling.

Free parameter	Prior	Limits
$\log(M_{\text{formed}}/M_{\star})$	Uniform	(9, 11.5)
A_V	Uniform	(0, 2)
Z/Z_{\odot}	Uniform	(0.1, 2)
τ/Gyr	Uniform	(0, $t(z_{\text{obs}})$)
α, β	Logarithmic	(10^{-2} , 10^{-3})
Noise rescale s_{noise}	Logarithmic	(1, 10)

Appendix A: Extended spectra of NS_274

For full transparency, we ran the customized `MSAEXP` pipeline also on the G140M and G235M spectra of NS_274. In this case, the advantage of extending the G140M spectrum is marginal compared with the gain obtained by processing the bluest spectrum of RUBIES-UDS-QG-z7 – simply because a deep coverage of the rest-frame optical wavelengths is already available. The G235M grating spectrum extension covers the $H\alpha$ Balmer line and the [N II] $\lambda\lambda 6549, 6585$ doublet. However, in the case of NS_274, the extension comes with an uncertain absolute flux calibration and a systematic color gradient compared with the PRISM spectrum. For reference, we re-ran the same pPXF modeling described in Section 3.1 and estimate a stellar velocity dispersion of $\sigma_{\star} = 278 \pm 23 \text{ km s}^{-1}$, 10% higher than, but in agreement with the value in Table 1. We also estimate observed (thus, magnified) line fluxes of [Ne III] = $2.8^{+2.6}_{-2.4}$, [O II] = $4.0^{+3.0}_{-2.8}$, $H\beta = 2.3^{+2.2}_{-2.3}$, [O III] = $8.9^{+2.6}_{-2.8}$, $H\alpha = 15.4^{+3.2}_{-3.5}$, and [N II] $\lambda 6585 = 37.5^{+5.0}_{-4.9}$ all expressed in units of $10^{-19} \text{ erg cm}^{-2} \text{ s}^{-1}$. We stress that the flux calibration uncertainties, and especially the color term, influence the line fluxes and their ratios non trivially, as the stellar continuum absorption features have to be modeled in order to derive the line emission. This explains the difference in the $H\beta$ flux measurement and its ratio with [O III] ($\log([\text{O III}]/H\beta) > 0.37$ ratio at 3σ in the extended spectrum). At face value, we estimate $\log([\text{NII}]/H\alpha) = 0.39^{+0.13}_{-0.11}$ (where the uncertainties are purely statistical), which would place NS_274 beyond the extrapolation to $z = 4$ of the line dividing star-forming galaxies and AGN in the BPT diagram (Baldwin et al. 1981) presented in Kewley et al. (2013). We note that the parameterization in Kewley et al. (2013) is not calibrated against data at $z = 4$ and should be taken with a grain of salt. If confirmed, these emission line ratios could support the possible presence of a faint AGN- or, at least, non-SF powered ionized emission as first proposed in Wu (2024). Future deeper observations will test this possibility.

Appendix B: Modeling supplementary material

In Figure B.1, we show the posterior distributions of the parameters obtained by modeling the spectra and photometry of NS_274 and RUBIES-UDS-QG-z7 as detailed in Section 3.1. Properties of the priors are reported in Table B.1. We show them in figure B.2. In Figure B.3, we report the results of the joint best-fit modeling of the G235M and G395M spectra of RUBIES-UDS-QG-z7 to determine its exact spectroscopic redshift (see Section 2.2). Finally, Figure B.4 shows the NIRCam/F200W image of NS_274, the best-fit Sérsic described in Section 3.3, and the residuals.

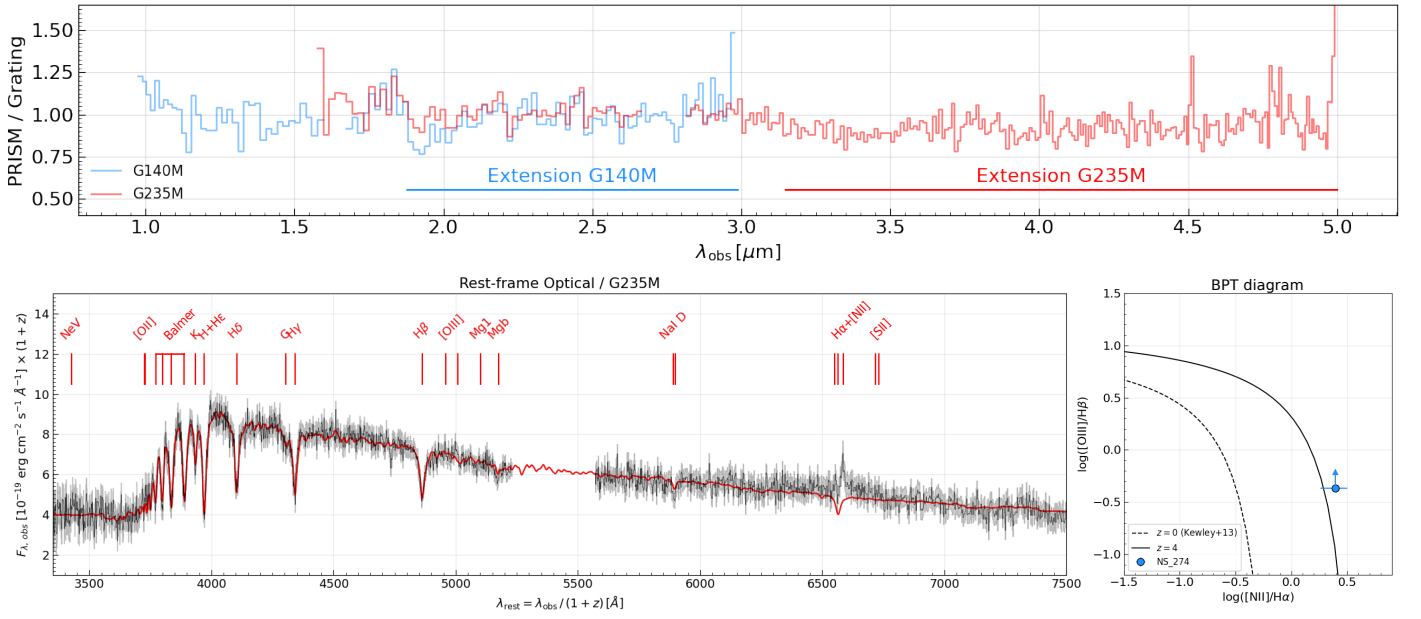


Fig. A.1. Top: Flux density ratio between the PRISM and G140M (blue line) and G235M (red line) grating spectra in the custom reduction of NS_274. We marked with a solid line the extended wavelength coverage. *Bottom:* Extended G235M spectrum of NS_274 (black) and its uncertainties (gray). The red line indicates the best-fit pPXF model of the stellar continuum. The panel on the right shows the location of the source in the BPT diagram based on the measurements in the extended G235M spectrum. The black dashed and solid lines indicate the empirical parameterization of the line dividing star-forming galaxies and AGN by Kewley et al. (2013) at $z = 0$ and $z = 4$, respectively.

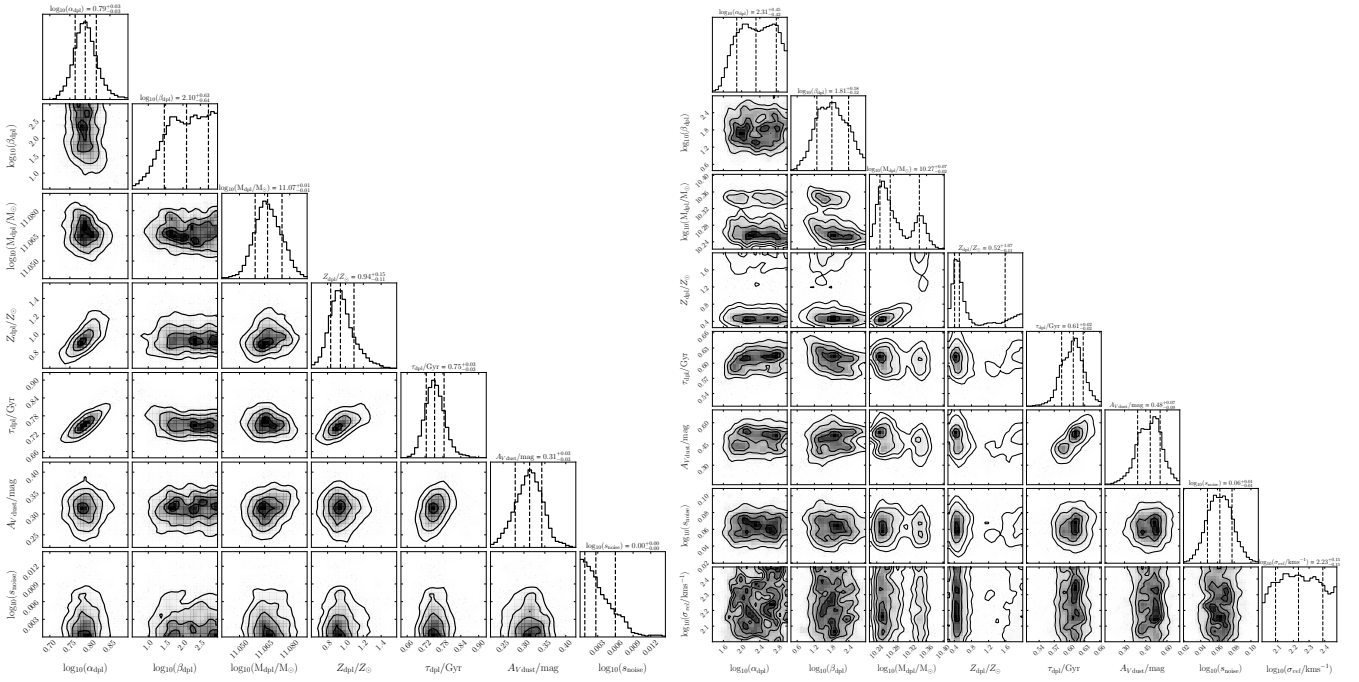


Fig. B.1. Corner plots showing the posterior distributions of the parameters constrained with Bagpipes as detailed in Section 3.1. Left: NS_274 at $z = 4.1061$; Right: RUBIES-UDS-QG-z7 at $z = 7.2758$.

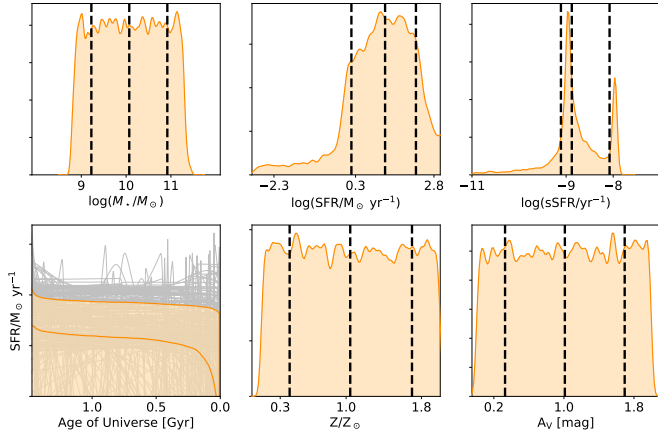


Fig. B.2. Priors on the parameters listed in Table B.1 for NS_274. Dashed black lines indicate the 16, 50, and 84% percentiles of the distributions. In the SFH panel, we show randomly extracted SFHs in gray. The orange area shows the 16-84% interpercentile range. Similar priors were applied to model the spectrum and photometry of RUBIES-UDS-QG-z7.

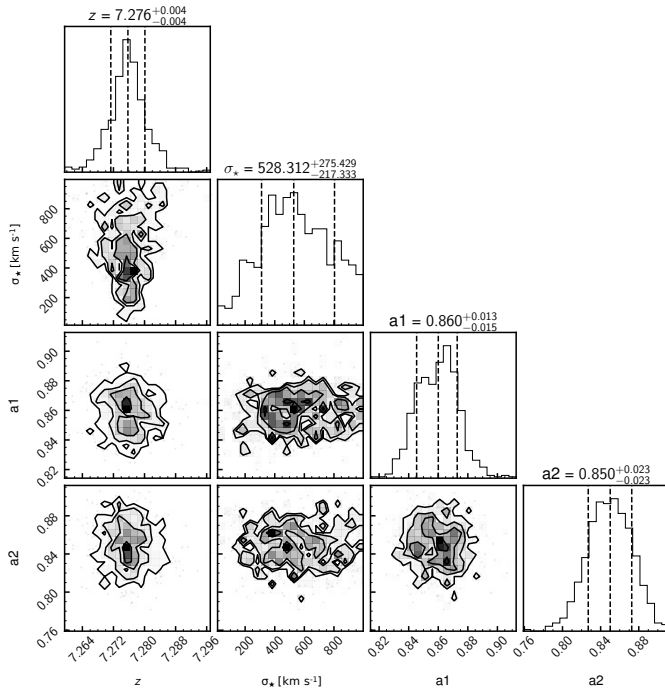


Fig. B.3. Corner plot showing the posterior distributions of the free parameters of the template scaling used to determine the redshift of RUBIES-UDS-QG-z7.

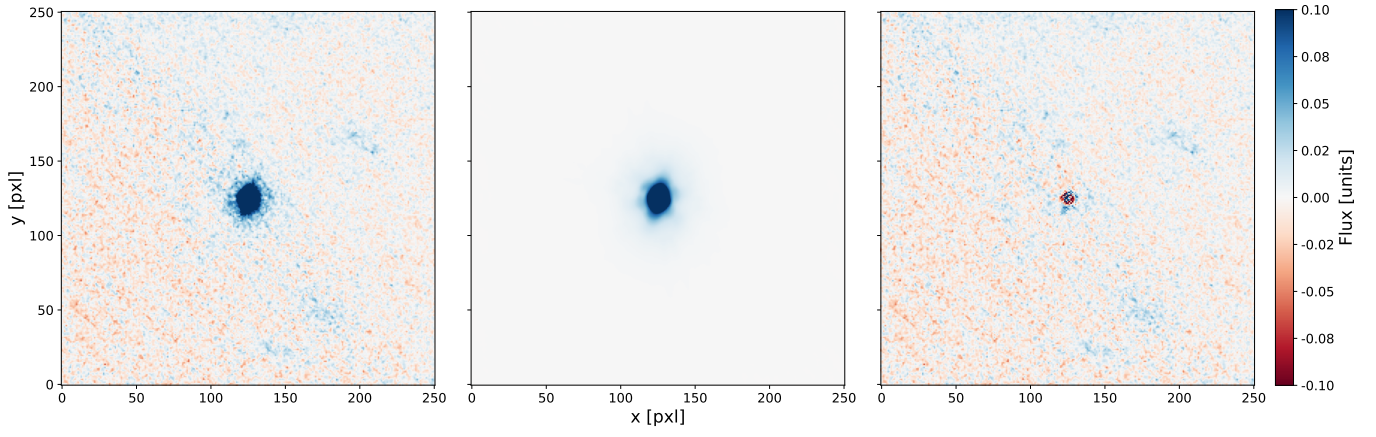


Fig. B.4. Sérsic modeling of NS_274. *Left:* $5'' \times 5''$ ($\sim 35 \times 35$ kpc at $z = 4.1$) F200W cutout image of our target. *Center:* Best-fit Sérsic model (Section 3.3). *Right:* Residuals computed by subtracting the best-fit model to the input image.